A Study of the Chemical and Physical Processes Governing CO_2 Laser-Induced Pyrolysis and Combustion of RDX

YOUNGJOO LEE,* CHING-JEN TANG, and THOMAS A. LITZINGER
The Pennsylvania State University, University Park, Pennsylvania 16802

The flame structure of 1,3,5-trinitro-1,3,5-triazacyclohexane (RDX) propellants under laser-assisted combustion was studied to better understand related chemical and physical processes in the gas phase. Experiments were conducted from 0.1 to 3 ATM in pressure with heat fluxes of 50 to 600 W/cm^2. Gaseous products were extracted through the use of quartz microprobes and analyzed by a triple quadrupole mass spectrometer (TQMS). Temperature profiles were measured using micro-thermocouple techniques to investigate reaction zones in RDX flames. Flame behavior was observed using a high-magnification video system. Major species in RDX flames were identified as H_2, H_2O, HCN, H_2CO, NO, HNCO, N_2O, and NO_2 at low masses ($m/z \leq 47$). In addition to these species, H_2CNH with $m/z = 29$ was found to exist in the near-surface reaction zone as an important minor species. Higher molecular weight species were found at m/z values of 47, 54, 56, 70, 81, and 97; with the daughter mode operation of TQMS, they were identified as HONO, $C_2H_2N_2$, $C_2H_4N_2$, $C_2H_2N_2O$, $C_3H_3N_3$, and $C_3H_3N_3O$, respectively. Increasing heat flux and decreasing pressure stretched out the reaction zones and were useful for investigating reactions near the deflagrating surface. However, the conditions appeared to have no effect on major reaction pathways. Two-stage chemical reaction pathways in the gas phase were explicitly identified from the major species profiles at all experimental conditions. Also, the reactions of minor high-mass species occurred in the primary reaction zone. The decomposition of RDX at the surface showed evidence of the two competing branch reactions into $H_2CO + N_2O$ and HCN + HONO, as well as two subsequent reactions: $H_2CO + N_2O \rightarrow H_2O + CO + N_2$ and $2HONO \rightarrow H_2O + NO + NO_2$. With the consideration of the previous four reactions, the branching ratio for the two decomposition pathways of RDX was estimated to be about 2:1. For all experimental conditions, temperature profiles had a near-surface region where temperature increased very slowly; the extent of this zone increased as the near-surface reaction zones expanded. After this region, the temperature profiles increased to final flame temperatures without any dark zone temperature plateau. Based on comparisons of species and temperature profiles, this near-surface region is believed to be related to the consumption of NO_2, production of NO and H_2O, and production and consumption of high-mass species.

INTRODUCTION

RDX (Fig. 1) is a highly energetic material widely used as a major ingredient of solid propellants in such applications as guns and rocket motors. Therefore, over the past several decades, many studies have been devoted to its ignition, decomposition and combustion behavior. In terms of decomposition and combustion behavior, research has generally been performed on two main decomposition regions: condensed (solid and liquid)-phase [1–12] or gas-phase regions [6, 8, 9, 11, 13–26]—while some studies focused on both regions [7–9, 27]. Two excellent reviews describe the major research accomplishments to date in these areas [28, 29].

Significant efforts have been devoted to identifying an initial stage of the thermal decomposition pathways in the condensed phase. Through RDX studies with gas chromatography/mass spectrometry (GC/MS) [2], mass spectrometry (MS) [3–5, 7–9], and spectroscopic diagnostics [6], it was found that RDX starts to decompose in the liquid phase, with little decomposition in the solid phase. Therefore, within reasonable accuracy, we could assume that the major decomposition occurred in the liquid phase [3]. The decomposition products identified in the solid phase were 1-nitroso-3,5-dinitrohexahydro-s-triazine (ONDNTA: $m/z = 206$) within the RDX lattice [3, 4], H_2 [9], H_2CO, and N_2O [3, 4, 9]. Major products evolved in the liquid phase, most of which were identified in MS studies [3, 4, 7–9], included H_2O, HCN, CO, N_2, H_2CO, NO, N_2O, NH_2CHO, NO_2, HONO, $(CH_3)NHCHO$, oxy-s-triazine (OST: $m/z = 97$), ONDNTA, and RDX vapors. However, among the studies, decomposition species and related reaction path-

*Corresponding author. E-mail: tal2@psu.edu

0010-2180/99/$–see front matter
PII S0010-2180(98)00119-9

Published by Elsevier Science Inc.

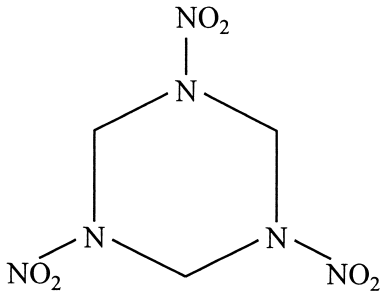

Fig. 1. Chemical structure of RDX.

ways in the condensed phase varied widely according to experimental conditions such as heating rate and diagnostics applied on the measurements.

In studies of the gas-phase decomposition of RDX, primary efforts were devoted to identifying gaseous products, investigating initial and subsequent decomposition pathways, and kinetic modeling and its comparison with experimental data. Literature dealing with initial decomposition products and subsequent chemical reaction pathways in the gas phase include studies using GC [6], MS [7–9, 15–20], photoelectron spectrometry [16], Fourier transform infrared (FTIR) spectroscopy [14, 17, 18, 21, 30], UV-VIS absorption spectroscopy [6, 17, 25, 31–33], and laser-induced fluorescence (LIF) [25, 31–33].

Initial decomposition products in the gas phase were reported to be H_2CNNO_2 from a symmetric triple concerted dissociation [13] or an RDX ring fragmentation [6, 9], NO_2 from the scission of N-N side chains [6, 8, 16–17, 19], or both H_2CNNO_2 and NO_2 [13]. There seems to be no consensus on initial gaseous products according to measurement methods or experimental conditions; therefore, this topic remains controversial. Major gaseous products evolved in the gas phase were identified as H_2, H_2O, HCN, CO, N_2, H_2CO, NO, N_2O, CO_2, and NO_2. However, some species that might have important roles in subsequent reaction zones in the gas phase, but were not commonly measured, have also been reported. They include H_2CNH [34, 35], HNCO [7, 15, 35, 36], HONO [13, 17, 30, 35], and N_2O_4 [21]. Experimental results become more diverse when the identification of gaseous products moves into high molecular weight species and intermediates of $m/z > 46$, such as $C_2H_2N_2$ ($m/z = 54$) [35]; $C_2H_4N_2$ (56) [9, 35]; $C_2H_2N_2O$ (70) [35]; $CH_2N_2O_2$ (74) [9, 13]; $C_3H_3N_3$ (81) [13, 35]; N_2O_4 (92) [21]; $C_3H_3N_3O$ (97) [35]; $CH_2N_3O_4$ (120) [13]; $C_2H_4N_4O_3$ (132) [9, 13]; $C_2H_3N_4O_4$ (148) [13]; and $C_3H_6N_5O_4$ (176) [13].

Although there are some discrepancies among initial and subsequent products evolved in the gas phase, two dominant reactions have been recognized as initial decomposition pathways in the gas phase of RDX pyrolysis that produce NO_2 + HCN and H_2CO + N_2O [14, 18, 37]. Reasonable agreement of quantities and trends for the major stable species have been obtained by comparing experimental and kinetic modeling studies [22, 23, 36, 38–41], but profound discrepancies still exist in the comparison of major radicals [42]. Therefore, we can state that the detailed mechanism of the decomposition is not clear since 1) various decomposition products depend on even slight changes of experimental conditions and setups, 2) many intermediates exist at the initial decomposition stage, and 3) several new species have been found by newly developed experimental systems.

RDX decomposition and subsequent reactions in the condensed phase are believed to be intimately connected to those in the gas phase. Therefore, the gas-phase chemistry and its relation to the physical behavior of RDX are important topics to be understood and modeled. RDX used in actual applications is a pellet-type propellant; however, a significant number of experimental results were obtained from its powder forms [6, 8–9, 13, 16–21, 25]. The data from this condition should be valuable for investigating fundamental chemistry of RDX, but they may be quite different from those from actual propellants, such as pellet-type propellants. Two research groups [Korobeinichev and his co-workers in Russia, and Hanson-Parr and Parr in Naval Air Warfare Center (NAWC)] have made significant contributions to the studies of decomposition and reaction pathways for the combustion of pellet-type RDX propellants. Korobeinichev and his co-workers studied combustion of RDX propellants under self-sustaining conditions using a time-of-flight mass spectrometer [7, 15, 36, 43]. Throughout the

measurements of gas-phase species and temperatures, they reported major species evolved from the deflagrating surface and thereafter suggested decomposition reaction of RDX and reaction pathways in primary and secondary reaction zones of the gas phase. Parr and Hanson-Parr employed a CO_2 laser for extensive studies of the laser-assisted combustion of nitramine propellants including RDX [24, 25, 31–33, 44]. The CO_2 laser was useful in identifying possible reaction zones near the surface, by expanding the flame zone through a radiative heat flux on the surface of propellant that simulated actual conditions. They made measurements of gas-phase species and temperature profiles to investigate chemical and thermal wave structures under laser-assisted combustion. Both groups succeeded in providing important chemical and physical data on RDX combustion; however, the first group could not identify the RDX flame structures under ballistic conditions, while the second group, despite their measurements of some important radicals and stable species, could only provide limited data of species measurements because of the inherent limitation of the measurement diagnostics applied.

Even though RDX flame structure under combustion is known qualitatively, a quantitative description of the chemistry in the flame has not been completely identified up to now. Mass spectrometry has been successfully applied to the study of flame combustion chemistry [7, 15–17, 19, 20, 43–47], thermal decomposition [8, 9], and dissociation mechanism and dynamics of RDX [13]. It has two advantages: 1) most radicals/species can be measured, which is very important for complicated flame chemistries, and 2) the measurement can be made with reasonably good spatial resolution. However, several species are frequently included at one mass to charge (m/z) value in the study of flames with mass spectrometry and cannot be differentiated with a single resolving sector MS. To differentiate species with the same mass, tandem mass spectrometry (MS/MS) has been used [48]. The TQMS system, which is based on the MS/MS approach and will be used in the present study, is capable of resolving several species with the same mass-to-charge value, the detailed features of which will be described in the "Experimental Approach" section.

The present study investigated the chemical and physical processes of RDX propellants under laser-induced pyrolysis and laser-assisted combustion, using a CO_2 laser to simulate the heat feedback of actual ballistic conditions. Major efforts were devoted to identifying and quantifying stable species and differentiation of species at a same m/z value, determining thermal wave structure, and comparing chemical and physical structures of RDX flames. The TQMS was applied to identify possible species at key masses and differentiate species at the same mass. Micro-thermocouple techniques were applied to examine the thermal wave structure in RDX flames by measuring temperature profiles. Flame behavior was examined with a high-magnification CCD camera and a video system.

EXPERIMENTAL APPROACH

Experimental Setup

The experimental apparatus is composed basically of a high-power CO_2 laser (used as the radiant heat source of RDX propellants), visual diagnostics for examining flame behavior and species sampling height, a TQMS and related electronics for gaseous-product analysis, and a data acquisition and analysis system. The schematic diagram of the experimental setup is shown in Figure 2.

The energy source for ignition and sustained combustion of RDX propellant samples was a Coherent Super 48 high-power CO_2 laser with a maximum of 700 W of continuous wave power. A series of silicon mirrors directed the beam from the laser to the test chamber through aluminum tubes that safely confine the high-power CO_2 laser beam. Before entering the test chamber, the beam passed through a drilled copper plate and then an expanding lens, both of which were mounted on sliding mounts movable on a vertical aluminum track directly above the test chamber. A 7 mm aperture in the center of the copper plate allowed only the more uniform center section of the beam to be passed on to the sample surface. A zinc selenide ex-

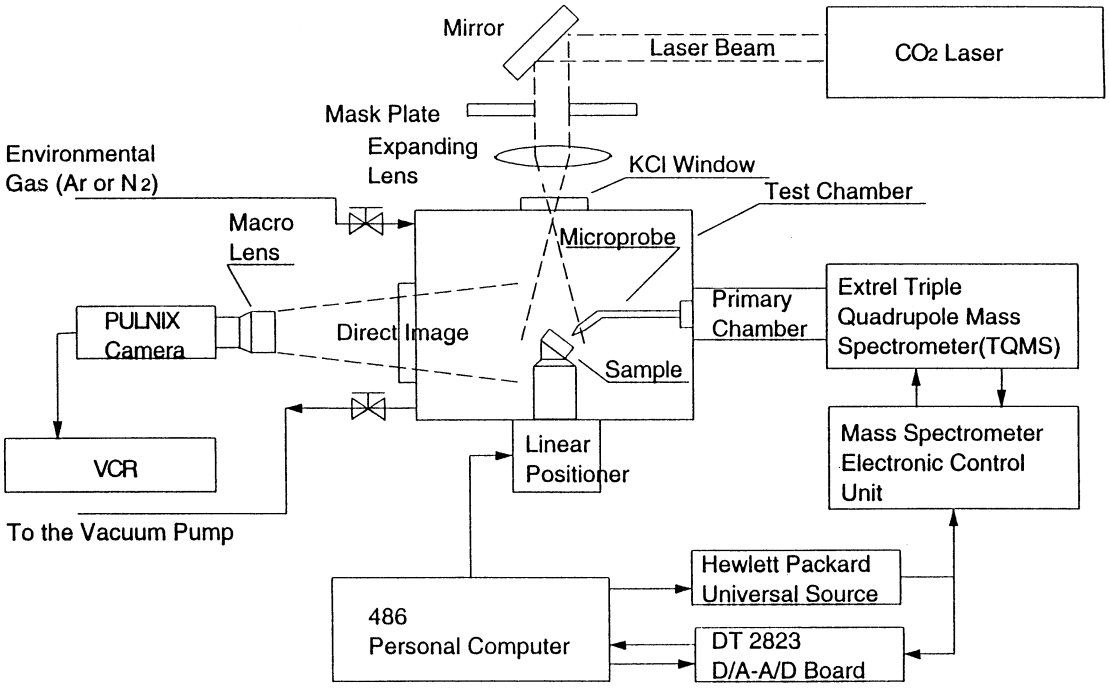

Fig. 2. Overall diagram of the experimental setup for the study of RDX propellants in the gas phase using a microprobe/triple quadrupole mass spectrometer (TQMS).

panding lens with a focal length of 24 cm could be moved on a track (not shown in the figure) to expand the beam to the desired area and thus obtain various levels of incident heat flux. The laser beam entered the test chamber through a KCl window and was applied to the propellant sample surface. The test chamber shown in Figure 2 was made from 1.3 cm-thick aluminum and was 25.4 cm tall and 16.5 cm wide, giving an internal volume of 4,460 cm^3. Four pipe-thread fittings were installed in the chamber to control the pressure and gaseous environment in the test chamber and data transmission. Two fittings allowed for gas flow from pressurized bottles containing the environmental gas (Ar or N_2) and provided outward gas flow induced by a vacuum pump. The other two fittings (not shown in the figure) were used to transport the photodiode and thermocouple signals out of the chamber. These fittings, purchased from CONAX Buffalo Co., were specially designed for sealing signal-transmitting wires.

The propellant samples were 0.64 cm (0.25") diameter pellets pressed from RDX powder by an in-house pellet presser. For a test, the propellant sample was glued to a small sample holder, angled at 45° to the incident laser beam so that the sampling microprobe could approach the sample perpendicular to its surface's center. This sample holder was attached to a linear positioner from Industrial Devices Corp., which permitted precise vertical positioning and movement of the test sample with respect to the position of the sampling probe orifice. During a test, the sample is pushed toward the sampling probe by the linear positioner to obtain species profiles versus height from the sample surface. A high-quality Plexiglas window was installed on one side of the chamber for direct-image photography of the RDX flame during combustion. The direct image was acquired using a Pulnix video camera with a Nikon macro lens and recorded with a professional VCR model BV-1000 from Mitsubishi Inc. Magnification of 30 to 40 times was normally employed to record images of flame structure and obtain the sampling height with the spatial resolution of about 20 μm. The recorded images were examined frame by frame to identify the sampling height with the help of separately recorded photodiode

signals. An infrared photodiode, installed in a corner of the test chamber, was used to identify the onset of the sample flame and observe the luminosity of the burning propellants.

Sampling of gaseous species was performed using a microprobe/mass spectrometer (MPMS) system. With this system, the time for the gas samples to pass through the microprobe and arrive at the MS ionizer is estimated to be about 10 ms (Mach number ~0.1). Therefore, compared with molecular-beam sampling, this microprobe sampling technique has a serious disadvantage of possible decomposition of the sampled species in the gas-phase and on the probe walls. To estimate the significance of the effects, the sampled gases in the probe were modeled as a one-dimensional, laminar, steady, reacting flow of a premixed gas mixture at a constant pressure. The calculation was performed at severe conditions within the probe: 1 torr in pressure and 1600 K in temperature. From the analysis, NO_2 was found to be the most reactive species; however, its maximum change was about 5% of its initial value in the calculation. The possibility of the reaction of the sampled species on the probe wall was also considered. From the literature, it was found that the main effects likely to influence the accuracy of the measurements are rapid quenching and catalytic effects [49]. Major plausible reactions were found to be NO_2 dissociation, NO oxidation to NO_2, and the oxidation of CO to CO_2, due to radical recombination reactions on the wall. However, the possibility of reactions seems to be low due to the canceling effects in the relevant reactions, for NO_2 and NO [49a–d], and the low pressure in the microprobe, for CO to CO_2 [49a, e]. Therefore, it could be reasonably assumed that there was little gas-phase reaction of the sampled species in the microprobe and on the probe walls. The same conclusion can be easily drawn for the high-mass species measured in this study since they appear near the sample surface where temperature was much lower than the value chosen in the modeling.

The species were sampled with a quartz microprobe with an orifice diameter of 20–30 μm, an outside diameter of 75–100 μm, and a nozzle half angle of 15–20°. The microprobe was constructed with quartz tubing of 2.0 (I.D.) × 3.2 (O.D.) mm from Quartz Scientific Inc., which was placed in a lathe and spun at low rpm while being heated with a small torch and pulled to create a narrower neck. The tubing was then cut at the narrowest point, and the tip was carefully ground back until an orifice of the desired size was obtained. The sample gases were drawn into the MS by a set of turbomolecular and vacuum pumps and ionized by electron impact in the MS. The mass spectrometer unit, a C-50 TQMS from Extrel, is capable of analyzing gaseous species in the mass range of 1–500 amu (atomic mass unit) with optional high-mass analysis power. It has a variable scan speed between 0.2 and 1,000 amu/s. A resolution of 8,000 is obtainable at a mass of 500 amu and 4,000 at 28 amu, and the sensitivity is 4 ma/torr at mass 28 amu before electronic amplification.

A two-stage pumping system was employed to obtain the required low pressures for the MPMS system. The vacuum conditions for the primary and secondary probe chambers of the TQMS system were achieved with a mechanical backing pump from Leybold and two turbomolecular pump units from Balzers. The mechanical pump evacuates the primary chamber from atmospheric pressure in the test chamber to about 0.1 torr with a 25 μm diameter microprobe. The secondary probe chamber containing the TQMS unit was pumped down to a pressure of about 10^{-6} torr for normal sampling conditions. A Pirani gauge and a cold cathode gauge were used to measure the pressures in the primary and probe chambers, respectively. The vacuum housings and flanges that house the TQMS and seal the MPMS system were purchased from MDC Vacuum Products Co. The ionized gas samples were directed to the detection system of the TQMS, where they were detected and the signals were amplified. The data were collected and analyzed using a 486-based personal computer and custom analysis software.

Species Measurement and Analysis

Identification of species and differentiation of several possible species with the same mass-to-charge ratio (m/z) value were performed using the TQMS. Two modes could be selected for the mass filtering operation of a C-50 TQMS:

parent mode and daughter mode. In parent mode operation, which is the same as single quadrupole mass spectrometer (QMS) operation, the existence of a gaseous species was identified by peaks at various mass values which were detected using only the first (Q1) or third (Q3) quadrupole mass filters of the TQMS. However, if multiple species exist at a given mass, differentiating these species is very difficult using only the parent mode; it requires multiple runs at different ionization energies or the application of a matrix approach for obtaining quantitative data. Therefore, daughter mode operation with the use of all functions of the TQMS is especially useful for differentiating and identifying several species with the same mass.

In daughter mode operation, the first quadrupole mass filter (Q1) is operated in a "single ion" mode, in which only the ions of interest are allowed to pass on as parent ions. The selected parent ions undergo dissociation through the process of collision-induced dissociation (CID) in the second mass filter (Q2). Argon was used as the collision gas in this study to minimize its contribution to fragmented masses. Several possible fragmented mass ions, called daughter ions, are produced and delivered into the third mass filter (Q3). Here, all possible daughter ions for each parent ion were scanned and directed into the detection system as in the parent mode. Two different types of daughter mode experiments were performed with different levels of collision energy; they will be referred to as the high and low collision-energy modes [48].

In the high collision-energy mode, the collision energy is sufficient to break double or even triple bonds of the parent ion. In the low collision-energy mode, the energy is only enough to break the weakest bonds of the parent ion, so that daughter ions deprived of small numbers of atoms are produced. The low collision-energy mode operation was especially useful when more than three species were possible and/or several hydrocarbon compounds could exist at the same mass. Based on the two sets of daughter mass ions for each parent mass, the most appropriate chemical formula of the parent mass was then deduced from the comparison of daughter ion patterns between the measured parent mass and a presumed chemical species, literature published on the propellants, and a library of mass spectra [50]. Based on the previously established procedures for identifying and differentiating species [34, 35, 51], the differentiation of species with the same mass was performed for mass 28: N_2, CO and C_2H_4; mass 29: H_2CO and H_2CNH; mass 30: NO, H_2CO, and C_2H_6; and mass 44: N_2O, CO_2 and CH_3CHO.

In the present study, experiments for RDX were conducted at pressures of 0.1 to 3 ATM and heat fluxes of 50 to 600 W/cm^2 during laser-assisted combustion. In reducing the species data, the measured concentrations were added together and each concentration was divided by the total to get the mole fractions of the sampled gases. (This method of calculating normalized mole fractions eliminates the effect of sample temperature on the observed signal intensities, since the temperature dependence cancels out. This method also cancels out the effect on signal intensity of probe orifice blockage during a test.) The measured mole fractions were then used to perform element balances through the reaction zones to check data quality.

Sensitivity Coefficients

Sensitivity coefficients of the measured species in the parent mode were acquired by several calibration methods. Most stable species were calibrated directly with the certified gas mixtures of known concentration. Water (H_2O) and acetaldehyde (CH_3CHO), which are liquid at ambient conditions, were heated and vaporized with the CO_2 laser to obtain sensitivity coefficients for their vapor states. This calibration test was conducted in 100% argon environment; therefore, any vapors evolved from either H_2O or CH_3CHO could be quantified with the comparison to argon depletion during the test. Paraformaldehyde, a polymeric solid of formaldehyde (H_2CO), was used to calibrate H_2CO. The calibrations of species for which standards were not readily available were estimated by correlating the signal intensity to that of calibrated species with a similar appearance potential through the ratio of their cross sections [52, 53]. However, when high-molecular-weight spe-

cies with a m/z value above 47 were measured, this cross-section method seemed to overpredict their sensitivity coefficients up to one order of magnitude and, accordingly, produced much smaller mole fractions. This was primarily due to the abundant fragmentation of an original species in the ionizer of MS; most of the original species was fragmented into lower-mass species, and only a small peak of signal intensity could be observed at the m/z value of the original species. Moreover, a species with the same number of atoms but slightly different structure from the real measured species gave very different sensitivity coefficients. Therefore, the use of the cross-section method in estimating sensitivity coefficients of measured high-mass species seems to misrepresent the actual quantities of the species.

Of chemicals with a structure the same as or similar to each high-mass species measured in present experiments, the only one available commercially was $C_3N_3H_3$ (triazine: $m/z = 81$). Therefore, $C_3N_3H_3$ was chosen as a standard for the prediction of sensitivity coefficients of other high-mass species. $C_3N_3H_3$, which is a liquid at the ambient condition, was vaporized under CO_2 laser heat flux for calibration. The sensitivity coefficients of other high-mass species were predicted by comparing their chemical structures with that of $C_3N_3H_3$, along with its distribution and pattern of fragmentation. However, since most of the high-mass species observed in this study were not measured in other experimental studies, they were not included when calculating mole fractions and element atom balance for measured species (see Fig. 13–16).

The calibration in the daughter mode was conducted with basically the same method described previously (parent mode using the daughter mode operation). For each parent gas species inserted in the calibration chamber, at least one distinctive daughter species was acquired. However, for parent species that showed common daughter species, each parent's calibration coefficient was derived from the proportionality of parents' contribution to the daughter species intensity. The calibration procedure was conducted under the same TQMS settings used in real experiments so that possible errors could be eliminated.

For all of the calibrations and actual tests, an ionization energy of 22 eV was used to minimize molecule fragmentation and get acceptable intensities. However, this setting was still high compared to the ionization energies of 9–15 eV for most organic compounds [54]; thus, some fragments were formed and contributed to the signals at masses other than the parent mass. In such instances, these fragment signals were subtracted from the mass signal of interest.

Temperature Measurements

Fine-wire thermocouples were used to obtain complete temperature profiles from subsurface to the final flame in the gas phase and investigate the structure of thermal wave in the reaction zones, as well as its relationship to the decomposition reactions. All temperature measurements were performed separately from species measurements. Various types of thermocouples were used to measure temperature profiles in different reaction zones. Although the maximum final temperature in the RDX flame could be close to 3000 K, the maximum temperature at the end of the primary flame zone was expected to be near 2000 K [25, 31, 51, 55–58]. Therefore, platinum/rhodium (Pt/Rh) and chromel/alumel thermocouples of small dimensions were used primarily for the condensed-phase and primary-flame temperature measurements. Because of their resistance to high temperatures, tungsten/rhenium (W/Re) thermocouples were used to measure the complete temperature profile of RDX flames.

Thermocouples were constructed using 25 μm-diameter platinum, platinum/rhodium, alumel, and chromel wires and 25 to 75 μm-diameter tungsten/rhenium wires. The wires were precisely welded together under a microscope with the electric spark method [59] to obtain the smallest bead possible. With a little practice, it was possible to obtain junction sizes the same size as the wire diameter or slightly smaller. W/Re thermocouples were fabricated using the same method, although the bead diameters were the same size as or somewhat larger than the wires. In the electric spark method, proper voltage and current levels were identified for each thermocouple type: 5–6 V and ~150 mA for 25 μm Pt/Rh and alumel/

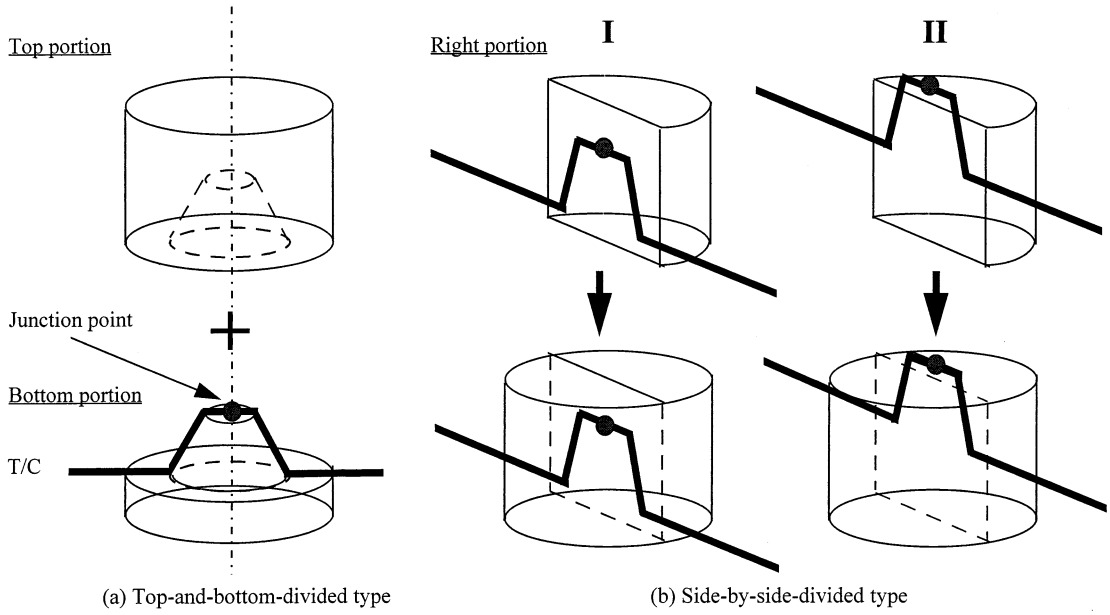

Fig. 3. Schematics of the temperature measurement setup for the near-surface region: (a) top-and-bottom-divided (TBD) type and (c) side-by-side-divided (SSD) type.

chromel thermocouples; 15–20 V and ~500 mA for 75 μm W/Re thermocouples. Thermocouple wires and prefabricated thermocouples were purchased from Goodfellow Corp. and Omega Engineering, Inc. Both Pt/Rh and chromel/alumel thermocouples were originally purchased from the Omega Company; however, the prefabricated thermocouples had bead diameters as much as three times the diameters of the wires and were large enough to decrease both spatial and temporal resolution of the measurement.

Two different configurations of the temperature measurement setup were constructed according to the temperature regions to be measured in flames. The first setup was a configuration with an embedded thermocouple (as shown in Fig. 3) to measure temperatures from the subsurface to the near-surface reaction zones in the gas phase. Two different types of configurations were considered in the measurement setup: top-and-bottom-divided type (TBD type) and side-by-side-divided type (SSD type). Originally, the TBD type was used to measure the near-surface temperatures; however, the recorded temperatures fluctuated widely. This was due to a void near the thermocouple junction point (see Fig. 3) produced by the incomplete joining of two pieces owing to dimensions of the imbedded thermocouple and the glue applied at the rim. Therefore, the SSD type was generally used for the near-surface temperature measurements and showed stable and repeatable values. Another configuration (II in Fig. 3b) for the SSD type was also used to identify measured profiles very near the surface. In this configuration, the junction point was originally placed at 100–200 μm above the surface before measuring to avoid contamination by the liquid from the surface. This configuration was found to be very effective in identifying the very slow-growing temperature region of RDX very near the surface.

Thin rolled thermocouples were primarily used in the temperature measurements near the surface. All three types of thermocouples were applied to compare the measured values. Rolled thermocouples were fabricated with a custom set of rollers. After rolling, the thickness of the junction region for the thermocouples was about 5 μm for Pt/Rh and chromel/alumel types and 5–10 μm for W/Re types. The SSD-type thermocouples were previously constructed by Russian researchers with 5 μm-thick

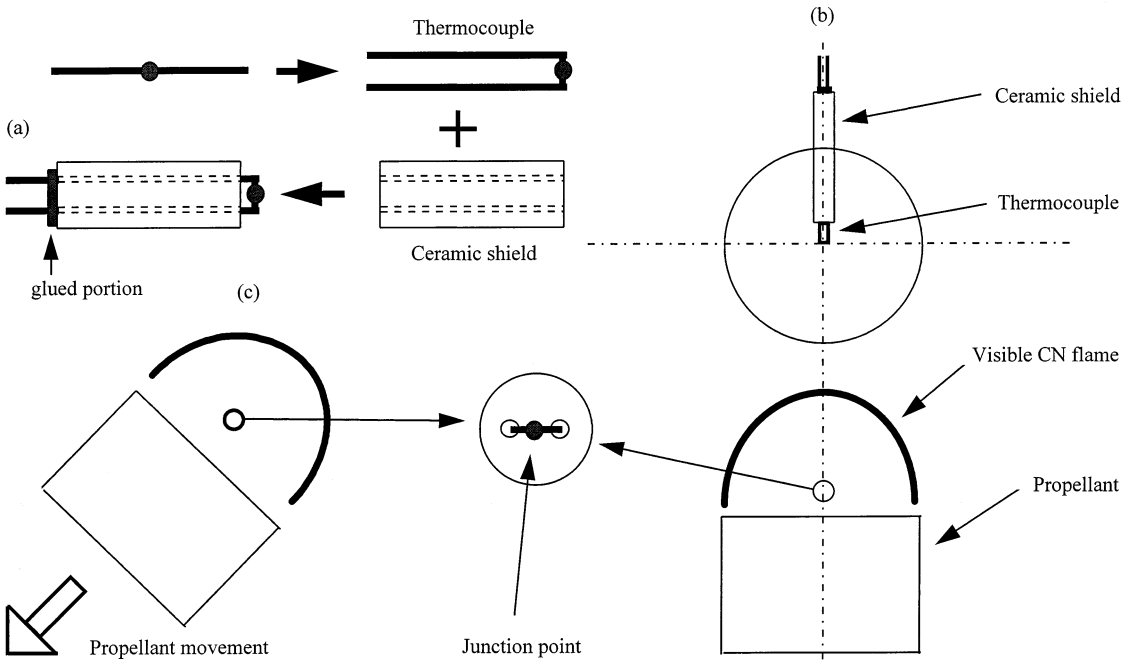

Fig. 4. Schematics of the temperature measurement setup for complete gas-phase profiles: (a) a process for making thermocouples with π-shape junction; (b) an application of the constructed thermocouples; and (c) temperature measurement in a real experiment.

rolled thermocouples using a spark welding method [56] and applied to the RDX gas-phase temperature measurements.

For measuring complete gas-phase temperature profiles of RDX, W/Re thermocouples with a 75 μm diameter were used to reduce the possibility of burnout during measurements. A special setup was designed for the measurements as shown in Fig. 4. The thermocouple was bent with a Π shape near the junction as shown in Figure 4a and inserted into two holes of the ceramic shield to protect the wires from the high temperature edge of RDX flames. The thermocouple wires were glued at the other end of shield holes as shown in Figure 4a to prevent the thermocouple junction from moving, and the whole setup was attached to a specially designed fixture (not shown in the figure). Therefore, only the junction point and part of the ceramic shield were inserted in the flame so that most of the wire was not heated. The dimension of the setup was small enough not to disturb the flame during measurements. During a measurement, the RDX propellant sample was moved downward and the thermocouple setup was fixed in space (as in Fig. 4) so that the thermocouple could pass through the flame. Moving the sample was also effective in stabilizing the flame and preventing it from attaching to the thermocouple junction point (which happens because W/Re thermocouples are very susceptible to burning in air).

A thermocouple immersed in a gas stream will record a temperature different from the true stream temperature due to several error sources [59]: thermocouple size and aerodynamic, thermal, and chemical effects. The effect of thermocouple size, reflected in the response time, was considered by converting all measured temperatures to be equivalent to those for 5 μm thermocouples. The aerodynamic effect, resulting from the velocity of the combustion gas stream, was not considered in this study, since the velocity was of the order of 5 m/s and therefore not high enough to affect measured values. The thermal effects due to radiative and convective heat transfer on the temperature measurement were calculated through the en-

ergy balance at the thermocouple junction using reasonable thermal properties similar to the actual gas environment [60, 61]. From the calculation, the magnitude of radiative heating term in the equation was found to be negligible compared with that of convective term; therefore, it was not included in the calculation. Conduction losses were also ignored since the thermocouple wires in these measurements were aligned with the surfaces of constant temperature. The most serious effects seem to come from the potential catalytic reactions on the thermocouple surfaces, since these effects result in spuriously high temperature and hysteresis in the temperature profiles [59]. Even though the considerations related to the reactions are very complicated, the catalytic effect can be made negligible by coating with noncatalytic materials. In an experimental investigation by Zenin, the temperature difference between uncoated and coated W/Re thermocouples was known to be small [62]. Therefore, this study gave no consideration to the catalytic effect.

The measured thermocouple signals were amplified by a six-channel wideband preamplifier before being recorded on the oscilloscope, with a gain of 50 dB that amplified the original signals about 316 times. A Nicolet NIC-310 digital oscilloscope was used to record the thermocouple signals. The scope operates at a maximum recording speed of 1 MHz and has two input channels—one for thermocouple signals and the other for photodiode signals. The photodiode signals were recorded simultaneously with the temperature signals to synchronize the video images of the flame to the temperature measurement; they were precise enough to pinpoint the exact time the visible RDX flame appeared. By cross-checking the signals and the RDX flame recorded in video, it was possible to identify the height changes of the junction point above the deflagrating sample surface during the measurement. The oscilloscope was triggered by a signal output from the CO_2 laser at the point of laser trigger, signaling the zero-time for the test. Two 3.5" DOS-compatible disk drives are included in the oscilloscope for signal recording, and two recorded signals were stored on disks right after the experiments for future analyses. The recorded temperature data were processed using VU-POINT software. Temperatures for Pt/Rh and chromel/alumel thermocouples were derived from voltage signals converted into temperatures by conversion programs, based upon manufacturer's specifications. Temperatures measured with W/Re thermocouples were interpreted with an equation derived from values in a conversion table from OMEGA [60].

RESULTS AND DISCUSSION

Differentiation of Species in Low Masses ($m/z < 46$)

From the results of previous research on RDX [63], some masses were found to include more than one species: N_2 and CO at mass 28; NO and H_2CO at mass 30; N_2O and CO_2 at mass 44. However, mass 29 was another challenge because it was possible that CHO, an ionization fragment from H_2CO, was not the only species at this mass. Therefore, using the TQMS, the possible species were differentiated and identified in the daughter mode. Details of the procedure to differentiate species in each mass are described elsewhere [34, 51]; therefore, only the results are summarized here.

The profiles of N_2 and CO in mass 28 vs height from the surface are shown in Fig. 5 [34], which also shows the effect of pressure and heat flux. The zero point of the figures in this study represents the liquid-gas interface. The liquid phase in the present study actually represents a thin layer of the mixture of vapor bubbles and liquid from RDX and its decomposed species on the propellant surface; therefore, it is defined as "two-phase region" and this term is used thereafter. In the figure, the expansion of reaction zones was clearly evident with decreasing pressure and increasing heat flux. The proportion of N_2 increased while that of CO decreased through reaction zones and became stable at the end. The trends of N_2O and CO_2 vs height from the surface are shown in Fig. 6 at three test conditions. N_2O constituted all of mass 44 at the surface without the existence of CO_2, but decreased gradually as the height increased. At the end of the reaction zones, all of mass 44 was composed of CO_2, one of the final products of combustion. The expansion of reaction zones as heat flux increased and pres-

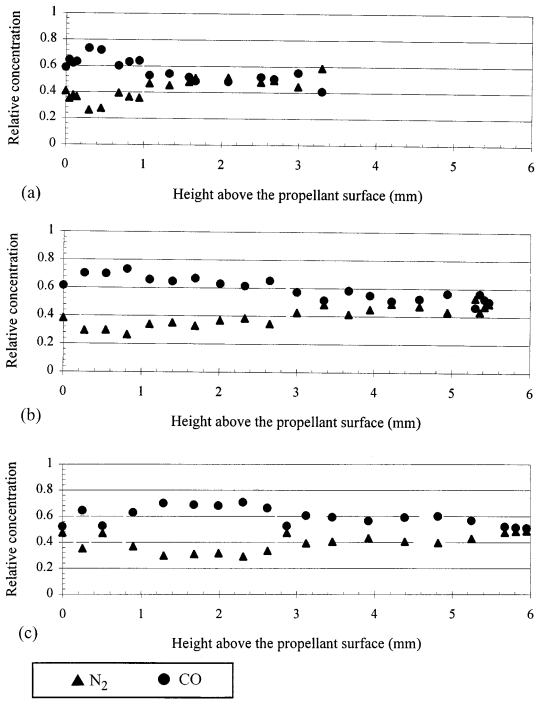

Fig. 5. Relative concentration of species at mass 28 for RDX in the conditions of (a) 1 ATM and 100 W/cm^2, (b) 1 ATM and 400 W/cm^2, (c) 0.5 ATM and 400 W/cm^2.

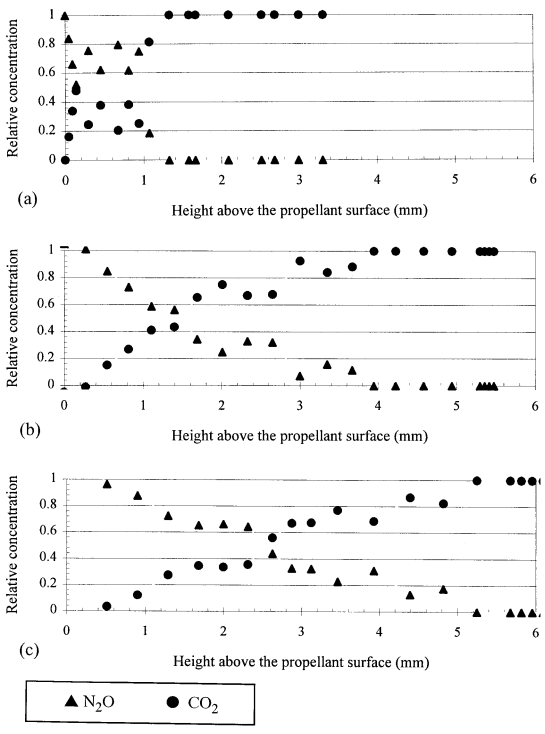

Fig. 6. Relative concentration of species at mass 44 for RDX in the conditions of (a) 1 ATM and 100 W/cm^2, (b) 1 ATM and 400 W/cm^2, (c) 0.5 ATM and 400 W/cm^2.

sure decreased is clearly visible from both species profiles.

Species with mass 29 and 30 were found to be highly correlated in the actual experiments as well as in the calibration of expected species [51]. In previous experiments with a single quadrupole MS [19, 20] in this laboratory, mass 29 was selected to identify H_2CO with the assumption that mass 29 is composed exclusively of CHO, based on the result of H_2CO parent calibration [34, 51]. However, some questions have been raised regarding the mole fraction of H_2CO near the surface of deflagrating RDX obtained from mass 29 because, in another study, the mole fraction of H_2CO was reported to be almost zero near the surface [25]. The fact that the H_2CO at the surface was not zero in this study supplied the motivation to perform experiments in the daughter mode for the parents at mass 29 and 30.

Figure 7 shows daughter mass results from an actual experiment for mass 29. From the calibration of CHO in Figure 8, mass 13 (CH) and 12 (C) were identified as the only possible daughters with a small amount of mass 16 if only CHO existed at mass 29. In the actual test at 1 ATM and 100 W/cm^2, however, a large signal at mass 14 was detected near the surface. Possible chemical species should be just CH_2 or N for mass 14, and other possible parent masses could be H_2CNH or C_2H_5, a radical which would have to come from fragmentation of C_2H_6, mass 30, in the ionizer. However, C_2H_5 was eliminated as a possible species because it would form from C_2H_6, which was not found in mass 30 in RDX experiments. Therefore, it could be deduced

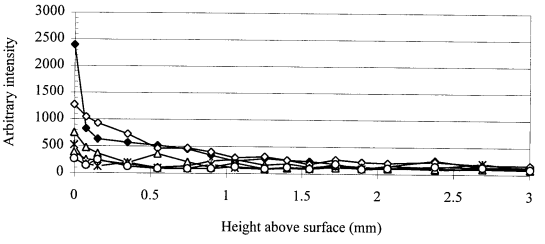

Fig. 7. Intensities of daughter-ion signals in the condition of 1 ATM and 100 W/cm^2 for mass 29.

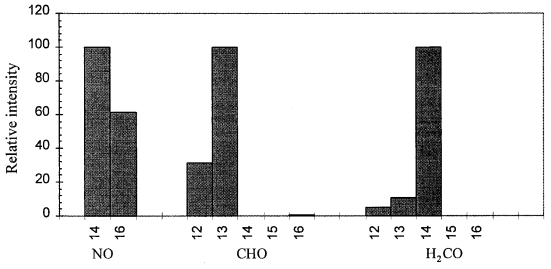

Fig. 8. Intensities of daughter-ion signals for the calibration of parent NO, CHO, and H_2CO in the high collision-energy mode. All tests were performed at 1 ATM and in N_2 environment.

that the mass 15 is more plausibly NH than CH_3. From this fact, it was concluded that the most likely species which satisfied the previous reasoning and contained N (mass 14) was H_2CNH with the following chemical structure:

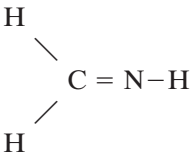

The fragments of mass 14 and 15 are highly likely from H_2CNH, because the energy produced in CID process in the high collision-energy mode is strong enough to break double or triple bonds and, although abundant fragmentation usually happens in the CID process, there are some preferences in the fragmentation patterns of a parent ion (see Table 1 and related literature in [48]). The radical H_2CN has already been suggested as an important intermediate species to form HCN [22, 23, 41], and H_2CNH has been also referred to as a possible intermediate species [40, 64]. However, both species were suggested only by modeling studies, and no measurement of the species has been reported. If H_2CNH is an RDX fragment, signal(s) from the counterpart fragment(s) from RDX decomposition should also be detected in species measurements. Considering the structure of RDX as in Fig. 1, possible candidates for the counterparts are $C_2H_2N_2$ (m/z = 54), $C_2H_4N_2$ (56), or $C_2H_2N_2O$ (70), as in Fig. 1. However, the distance of the total consumption for any of these species (see Fig. 12) does not coincide with that of H_2CNH (see Figure 10) at either of the two different pressure conditions. Although the distance of $C_3H_3N_3O$ (m/z = 97) in Fig. 12 seems to be similar to that of H_2CNH at the two pressures, $C_3H_3N_3O$ is not a structure that can be produced simultaneously with H_2CNH since $C_3H_3N_3O$ retains the ring structure of RDX and H_2CNH is from ring fragmentation. Therefore, the H_2CNH measured in this study can be considered an actual product.

TABLE 1

Daughter-Mass Ion Spectra for Parent Masses Measured Using the CID Process*

	High-energy mode		Low-energy mode	
	Major masses	Minor masses	Major masses	Minor masses
54	28	29, 30, 40		53
56	28, 29, 30	40, 42, 43, 44		50
70	30, 44	56, 43, 40, 42	44, 56, 43, 40	39
81	27, 28, 29, 55	54	80	69
97	26	56, 29, 70, 44, 46		79, 86

* Masses are in descending order.

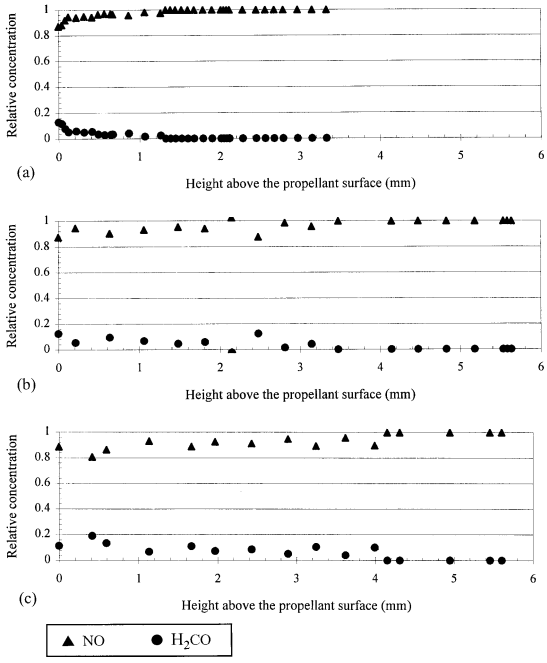

Fig. 9. Mass 30 for RDX in the conditions of (a) 1 ATM and 100 W/cm^2, (b) 1 ATM and 400 W/cm^2, (c) 0.5 ATM and 400 W/cm^2.

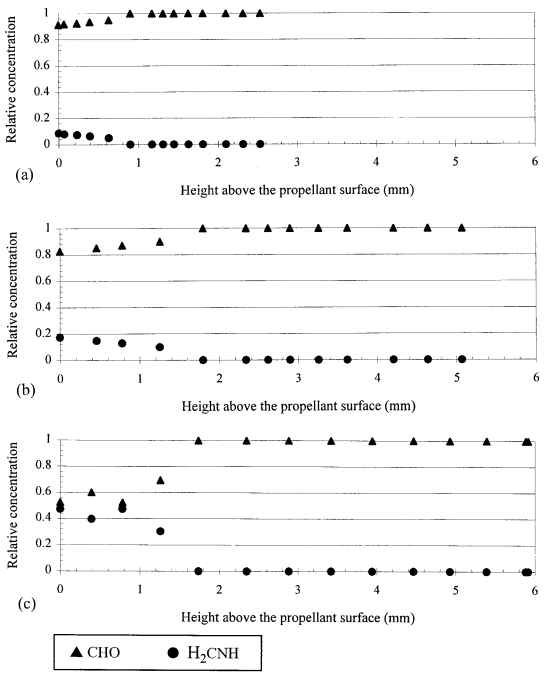

Fig. 10. Mass 29 for RDX in the conditions of (a) 1 ATM and 100 W/cm^2, (b) 1 ATM and 400 W/cm^2, (c) 0.5 ATM and 400 W/cm^2.

Trends of the NO and H_2CO contributions to mass 30 are shown in Fig. 9 at three different conditions of heat flux and pressure. NO constitutes most of mass 30 in the primary flame zone and all of it after this zone. The existence of H_2CO in the primary flame was clear at every experimental condition from the figure. Figure 10 shows the trends of CHO and H_2CNH in mass 29; H_2CNH was found to constitute a considerable portion of mass 29. However, its existence was identified only near the surface. By use of a calculated sensitivity coefficient, the maximum mole fraction of H_2CNH was estimated to be about 1% at the surface for the condition of 0.5 ATM and 400 W/cm^2. The quantity of H_2CNH was estimated by the cross-section method (see "Sensitivity Coefficients"). Although it was an ionization fragment, the mole fraction of CHO was presented in Fig. 10 for comparison of its magnitude with H_2CNH in mass 29. The mole fraction of CHO was estimated from the intensity of its daughter mass 13 (CH) rather than from the measured amount of CHO after the deduction of H_2CNH in mass 29.

Identification of Species in High Masses ($m/z > 46$)

Initial decomposition products of RDX have been recognized as important for determining the initial gas-phase decomposition pathways [6, 8, 9, 13, 16, 17, 21, 35]. Therefore, identifying the high-molecular-weight products is important to elucidate the initial decomposition of RDX. A major portion of the initial products in the gas phase are composed of high-mass species of $m/z > 46$, which are not well studied. Regarding this topic in the present study, two main questions exist: 1) how many real decomposition products exist, as opposed to ionization fragments, among the measured masses, and 2) what are their chemical structures? These two questions are the main themes to be investigated in this section.

Intensities of masses at m/z values are measured for each experimental condition. The parent masses were identical for all conditions: 47, 54, 56, 70, 81, and 97. No species over 100 were measured. Masses 56 and 81 measured here were reported previously in a gas-phase decomposition study of RDX to identify its decomposition pathways through infrared multiphoton dissociation (IRMPD) [13]. However, while masses 47 and 97 were found in this study for masses lower than 100, masses 74 (methylenenitramine), 82, and 83 were measured in the IRMPD study [13]. Therefore, although both studies were conducted for investigating RDX gas-phase decomposition at high heating rates, significantly different high masses were measured in the two experiments. Since most of the high masses measured in this study showed their maximum intensities at the surface, it may also be appropriate to compare the masses with condensed-phase decomposition products in other studies [3–5, 9]. However, many of the higher masses in the present study were also different from the masses measured in the liquid-phase decomposition studies; the only coincident masses were 70 and 97 [3–5] or 56 [9]. This difference seems to result from the substantial difference in experimental conditions. For all of the high-mass species evolved from the surface, attempts were made to differentiate the actual products of RDX decomposition from fragments formed by ionization [34,

51]. By varying the ionization energy from 22 to 14 eV, it was found that the species at masses 47, 54, 70, 81, and 97 are considered true decomposition products of RDX from relatively small changes of their profile trends and peak-point intensities [51]. However, the contribution of fragmentation to the signal at mass 56 was found to be significant, and no higher masses such as 70, 81, and 97 could be contributing this signal. Therefore, most of the signal intensity for mass 56 seems to be produced by the fragmentation in the ionizer from a higher gaseous product above the m/z of 97. It may be RDX because RDX was measured at similar experimental conditions [31], or may not be RDX based upon the fact that no RDX fragments commonly measured in MS studies, such as masses 75, 120, 128, and 148, were observed in this study [3, 13]. Thus, the mass 56 signal implies, but does not show any decisive evidence for, the existence of RDX in the gas phase.

For the high masses observed in this study, there exists a high probability of multiple species for a given m/z value, based on the available mass spectra library [50]. However, since the RDX molecule has a rather unique chemical structure made up of only C, H, O, and N, possible combinations for the observed m/z value are limited. For all high masses, daughter ions were examined to determine which chemical structures of the measured high masses could be deduced from the measured daughter ions and whether they were consistent with the expected chemical structures given in the literature [3, 9, 13, 65–67].

Daughter-ion spectra for parent masses measured using the CID process are shown in Table 1. Several major and minor daughter ions were identified for each parent mass and classified based on the relative intensities. In the CID process, according to the structure of a parent-mass ion, the fragmentation patterns and the abundance of daughter ion species show some typical tendencies [48]. Using these patterns and the daughter ions, chemical structures related to the measured masses were suggested in Fig. 11 for each parent mass (except that of mass 97, where the intensities of measured daughter ions were too small to provide detectable daughter-mass signals). The structure of mass 81 was obvious since $C_3N_3H_3$ (triazine)

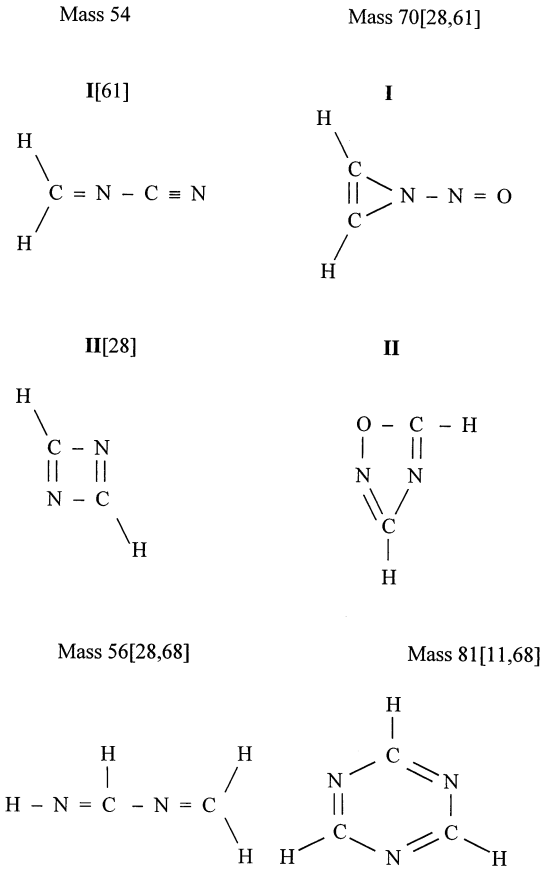

Fig. 11. Suggested chemical formula for each parent mass from the measured data in Table 1. The numbers in parentheses show related reference.

was commercially available; the daughter-mass ion spectra of $C_3N_3H_3$ was found to closely match that of the mass 81 from RDX. However, this kind of matching method could not be applied to other masses; the structures of other high molecular masses were obtained primarily from the measured daughter-ion spectra in Table 1, a database of daughter-ion spectra from parent species, and literature that previously reported related structures [13, 29, 63, 68]. The chemical structure II shown in Fig. 11 for mass 54 and 70 represents a less preferred structure based on the information of daughter ions produced in experiments. For example, at mass 54, the major daughter ions were measured at mass 28 and 29. In the CID process, most abundant daughter ions generally correspond to single-bond breaking. For structure I in Fig. 11, the

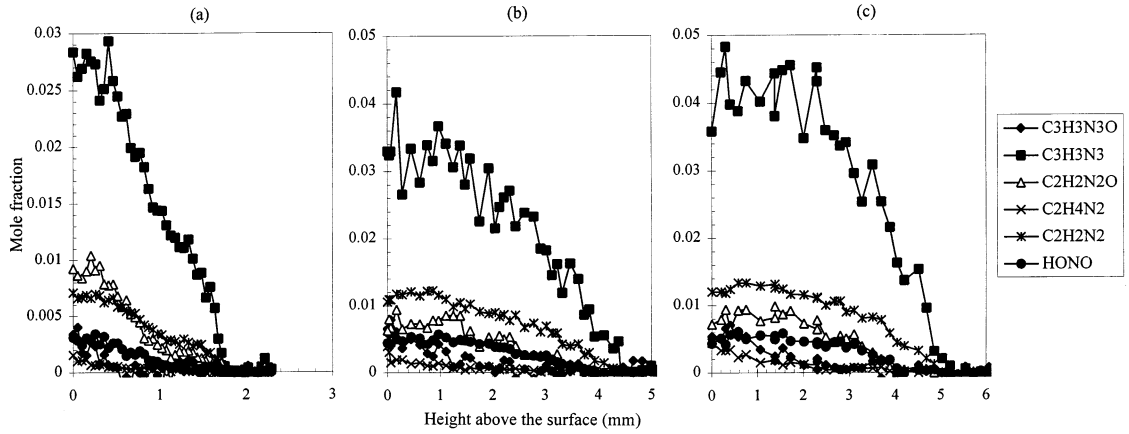

Fig. 12. Mole fraction of high-mass species identified in the gas phase of the deflagrating RDX at the conditions of (a) 1, (b) 0.5, and (c) 0.2 ATM and 400 W/cm^2 in argon environment. The height above the surface of RDX in each condition is the same as the species profiles in Figs. 14, 15, and 16, respectively.

production of daughter ions at mass 28 and 29 only requires a single-bond breaking of an N-N bond and a reattachment of H to the bond, respectively, whereas more complex breakings and reattachments are required for structure II. The same analysis can be applied to the structures of mass 70. It is interesting that all of the high masses measured in this study were also observed in HMX studies, but the daughter-mass ion spectra for each mass were not the same for the two materials at the same conditions [Table 1 and reference 69]. Although RDX and HMX are cyclic structures with the same basic chemical unit, H_2CNNO_2, it is possible that the decomposition products from the materials may not be identical.

With the sensitivity coefficients of $C_3N_3H_3$ measured and those of other high mass species estimated from $C_3N_3H_3$ as described in the "Sensitivity Coefficients" section, it was possible to quantify all high-mass species measured in this study. The mole fraction profiles of the high-mass species are shown in Fig. 12; the height above the surface for each condition was adjusted to the same as that in the lower mass species measurement of Figs. 14, 15, and 16, respectively. The structure of mass 97 could not be identified in this study, but was assumed to be $C_3N_3H_3O$ from other work [3]. From Fig. 12 for conditions of 1 to 0.2 ATM, some valuable facts could be deduced. Most of the high-mass species exist up to the CN flame and are consumed in the primary reaction zone (except $C_3N_3H_3O$ and $C_2N_4H_2$). Therefore, the consumption of these high-mass species constitute sources of the production of some major final products such as H_2, CO, N_2, and CO_2 in the dark zone. At every condition, $C_3N_3H_3O$ and $C_2N_4H_2$ always started to be consumed from the surface and before the dark zone; the consumption of these two species may explain the apparent production of other high-mass species near the surface. No significant improvement of element mole fraction was obtained after including the quantities of these high-mass species into related species profile at each condition; therefore, these species were not included in Figures 14–16.

Chemical Structure

Chemical processes in flames can be divided into two parts: *what* chemical changes occur under a given set of conditions, and *how fast* they occur [59]. The former question is related to the problem of specifying the mechanism or path of reactions during which the changes are taking place in flames. Therefore, it requires not only an understanding of related thermodynamics and chemical reactions, but also calculation of equilibrium flame properties (temperatures and species compositions). The question of how fast the reactions occur comprises the subject of chemical kinetics. In this study, interest is fo-

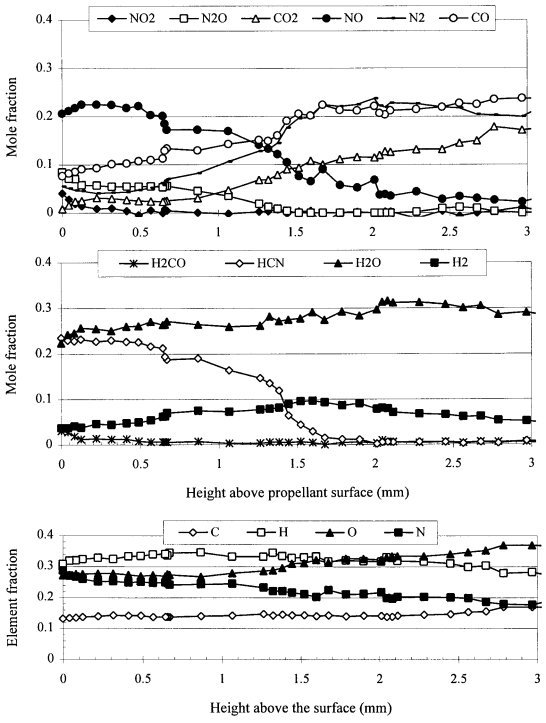

Fig. 13. Species profiles and element fraction profiles for deflagration of RDX at heat flux of 100 W/cm^2 in argon at one atmosphere.

cused on what chemical changes in flames are taking place; therefore, in the study of RDX decomposition, chemical species were measured to trace out the relationships between measured species and chemical reactions.

The results for major species at the condition of 1 ATM and 100 W/cm^2 are shown in Fig. 13. This condition was selected as a baseline for RDX species measurements since all the typical phenomena of RDX combustion were observed: stable regression, separated flame zones, and a relatively stable CN flame. Several experiments were actually conducted at this condition to acquire reliable data because it was found that the quartz microprobes could not withstand more than 400 ms above the final flame without melting. For protecting the microprobe from melting during experiments, the propellant sample was moved toward the microprobe so that the probe penetrated the final flame within 100 msec from the start of the test. The results shown in Figure 13 are representative species data in the gas phase at this condition.

Chemical reactions in the gas phase start with the consumption of H_2CO and NO_2 in the primary reaction zone very near the surface. Primary products of the consumption were H_2O, NO, CO, and CO_2. The following reaction has been generally accepted as the major heat release reaction in the primary flame zone [14, 27]:

$$5H_2CO + 7NO_2 \rightarrow 7NO + 3CO + 2CO_2 + 5H_2O \qquad (R1)$$

Reaction (R1) is considered a dominant pathway in producing heat at pressures up to 100 ATM and temperatures up to 700–800 K [27, 37]. However, due to the relatively high heating rates and low temperatures near the surface in this study compared to those in the FTIR studies, the consumption of N_2O was also noticeable at this condition (see Figs. 14–16). The temperature range in this primary reaction zone was estimated to be 600–850 K based on temperature measurements at other conditions (see Figs. 17 and 18). HCN and H_2 were relatively inert in this zone. While it is not included in (R1), the existence of N_2 at the surface should not be overlooked; N_2 has been reported to be produced directly from the condensed phase in several RDX experiments [9, 10]. The amount of N_2 produced at the surface was unaffected by the change of pressure and heat flux. This species was relatively inert in the primary reaction zone and became one of the primary products in the secondary flame zone.

Before continuing to the secondary reaction zone, the primary reaction zone was followed by a transition zone, or "inert zone." The inert zone in the species measurements is defined as the region in which most major species are relatively constant in mole fraction. Due to the relative inertness of two major reactants, NO and HCN, in the reaction zone, there is a distinctive profile discontinuity for the reactants at ~700 μm, the start of the secondary reaction zone, in Fig. 13. The length coincided with the violet CN flame distance in the video, which was also the standoff distance of the secondary (luminous) flame. It is noteworthy that the consumption of N_2O and H_2CO, which were not considered active in the secondary reaction zone in other studies [41, 70], is still present in

the secondary and inert zones at higher heat flux conditions (see Figs. 14–16).

The secondary flame zone has been characterized by the consumption of NO and HCN, and by the production of CO_2, N_2, CO, H_2O, and H_2 [2, 71]. In this experiment, the consumption of N_2O also produces N_2 in this zone [18, 20]:

$$N_2O, NO, HCN \rightarrow CO_2, N_2, CO, H_2O, H_2 \quad \text{(R2)}$$

The post-flame region appeared approximately 3 mm from the surface at this experimental condition. In this region, major products were identified as CO_2, N_2, CO, H_2O, and H_2, with a small amount of NO (~2%). Small signal intensities of N_2O, NO_2, and H_2CO were noticed in this region, but were within the range of noise fluctuation. The profile of each species in this zone fluctuated due to the fluctuation of the CN flame, which caused the tip of the sampling microprobe to move in and out of the flame.

At this experimental condition, the quantities of H_2CO and H_2CNH within mass 29 were distinguished (see section "Differentiation of Species in Low Masses"); however, no substantial improvement of the element fractions resulted in Fig. 13, compared to a previous result where mass 29 was not fully differentiated [34]. The relatively poor element fractions at this condition, high H and O, and low N suggest the need to consider the source of the discrepancy.

Based on the small gradients in concentration of all species measured at the surface, it was suggested that balancing the species composition in the gas phase using the element balance equation is a valid approach [19, 20, 63]. The poor element balance suggests that some major species might have been missed. However, this seems not to be the case because most major species reported for the RDX flame were measured, and some major radicals such as NH, OH, H, and CN, which were not measured, were reported to have low concentrations in the gas phase [17, 25, 36]. Even the high-mass species do not appear to be the reason for poor balance because 1) the imbalance increased away from the surface, 2) all high masses existed in the near-surface region, and 3) most identified high-mass species contained equal numbers of C, H, and N atoms, so that no improvement in the C, H, and N balances could be expected even after their inclusion in the element balance calculation. Moreover, although a more accurate species differentiation was accomplished to identify species in mass 28, 30, and 44, the element fraction did not improve for H and N (Fig. 13–16). Thus, the only other plausible source of the poor element balance is a calibration coefficient error. All calibration coefficients of major species used in this study were obtained at a standard condition of 1 ATM and 300 K; therefore, the coefficients away from the surface where the maximum temperature could reach up to ~3000 K are likely to be different from those at the standard condition. Since no data were available for the effect of temperature changes on calibration coefficients of major species up to the final temperature, no further attempt was made to correct the mole fraction of the measured species. It is noteworthy that, with the calibration coefficients obtained by the same calibration method as for RDX, species measurement results for other propellants, e.g. RDX composites [72, 73], showed better element balance results.

Other investigators have reported the gas temperature very near the surface of RDX to be in the range of 900–1100 K, and the surface temperature to be about 600–700 K [44]. Due to the high temperature gradient very near the surface, Russian investigators had suggested that a very thin reaction zone exists very near the surface of RDX, within 200 μm [15, 36]. This was not obvious at the test conditions shown in Fig. 13 because of the limited resolution near the surface. Thus, searching for this region was another reason to raise heat flux and lower pressure in order to get higher resolution in the region very near the surface and thus to identify this possible reaction zone.

Figure 14 shows the species profiles as the heat flux was increased to 400 W/cm^2 with the same pressure, 1 ATM. The sampling resolution was increased by keeping the sampling probe inside the CN flame longer and increasing heat flux. The chemical structure of the flame at this condition was similar to that at 100 W/cm^2. However, total reaction zone length did expand more than 5 mm from the surface based on the profile of NO from 3 mm at 100 W/cm^2. Based

on the point where NO stops increasing, the expansion of the primary reaction zone thickness was substantial: from ~200 to ~500 μm.

At the surface, the mole fraction of NO_2 was higher and that of N_2O was lower relative to the lower heat flux case, because N-N bond scission was preferred at the high heat flux condition. However, the trends of NO, NO_2, and N_2O profiles were practically unchanged as heat flux increased. This result showed that the change in heat flux might change mole fractions of major stable species at the surface, but did not have much effect on the chemical mechanisms near the surface. Two competing decomposition pathways have been suggested for the surface reaction zone [37]:

$$\text{RDX} \begin{cases} \nearrow 3\,(H_2CO + N_2O) & \text{at the low heating rate and low temperature} \quad \text{(R3)} \\ \searrow 3\,(H_2CN + NO_2),\ \text{or}\ 3\,(HCN + HONO),\ \text{or}\ 3\,(H\cdot + HCN + NO_2) & \text{at the high heating rate.} \quad \text{(R4)} \end{cases}$$

This narrow zone might be connected to the consumption of RDX because some production of high mass species was also found in this zone (see Fig. 12). From the profiles of major species (especially NO, N_2O, and HCN), the secondary flame zone was also identified to be stretched substantially compared with that at 100 W/cm^2. Even at 5 mm from the surface, NO and HCN were still being consumed. The abrupt change of species profiles at about 2.5 mm in Fig. 14 shows that the tip of the microprobe moved outside of the primary flame due to the unstable nature of the flame at this point during the experiment, which is not a typical or intrinsic phenomenon of RDX combustion. The element fraction at this condition also shows relatively poor agreement with the original formulation, the same as that of the lower heat flux in Figure 13. However, the value improved as it approached the surface. This will be discussed in more detail for the lower pressure results (Figures 15 and 16).

The species profiles in the gas phase at the condition of 0.5 ATM and 400 W/cm^2 are presented in Fig. 15. Because the combined effects of lower pressure and higher heat flux were employed in the experiment, the reaction zone near the surface was highly stretched. Therefore, the primary reaction zone was expanded to ~3.5 mm, and the secondary flame zone did not begin until about 4.5 mm from the surface, as indicated by the consumption of NO and HCN. The existence of another reaction zone very near the surface, which was suggested at 1 ATM and 400 W/cm^2 and expected from previous results [7, 15, 20], is still not evident at this condition in the species profiles of NO_2, N_2O, H_2, and H_2CO. The stretching ratio of the primary reaction zone between this condition and the case of 100 W/cm^2 at 1 ATM (Fig. 13) is estimated to be over 10, based on the profile of NO_2. However, when compared to the results at 1 ATM and the same heat flux (Fig. 13), more

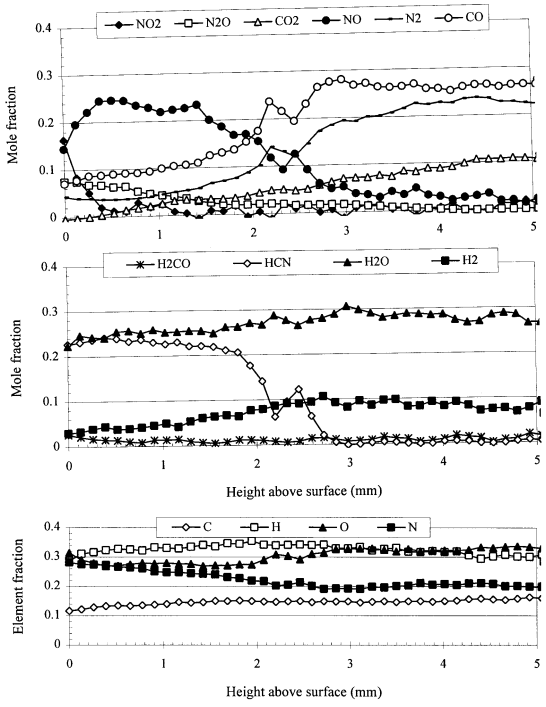

Fig. 14. Species profiles and element fraction profiles for deflagration of RDX at heat flux of 400 W/cm^2 in argon at one atmosphere.

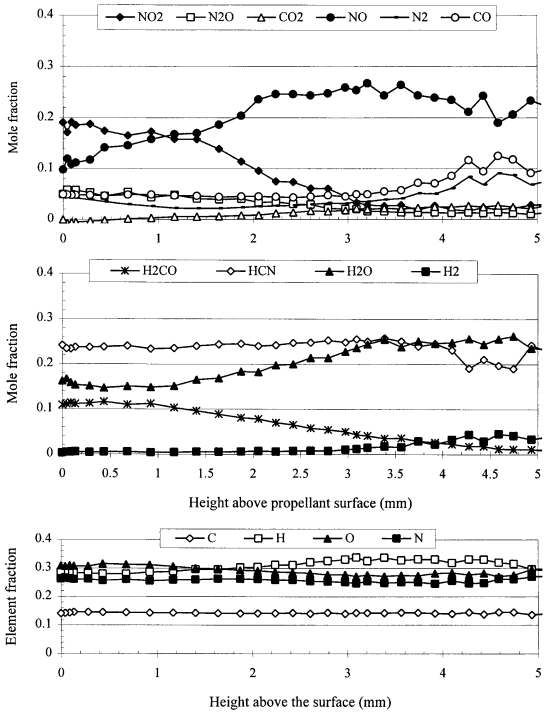

Fig. 15. Species profiles and element fraction profiles for deflagration of RDX at heat flux of 400 W/cm^2 in argon at 0.5 atmosphere.

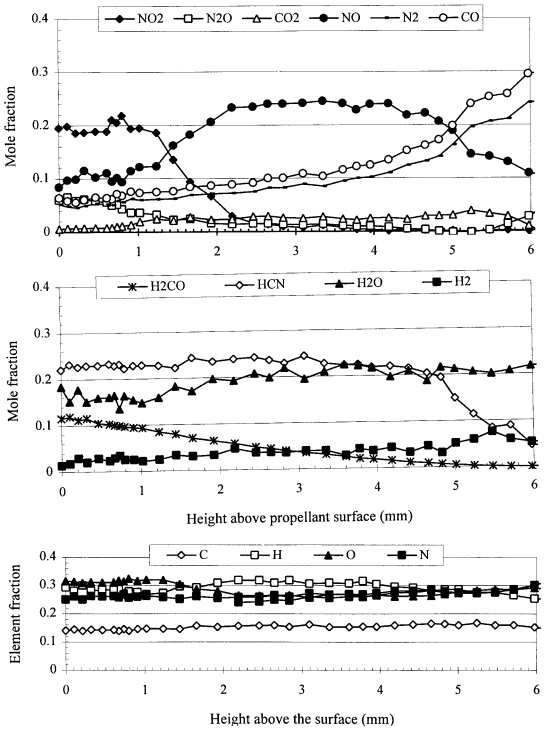

Fig. 16. Species profiles and element fraction profiles for deflagration of RDX at heat flux of 400 W/cm^2 and 0.2 atmosphere in argon environment.

NO_2 and H_2CO exist at the surface with little change in N_2O, which suggests that these two species have not yet reacted to form NO, and H_2O and CO, respectively. The mole fractions of most of species at 0.5 ATM changed very little compared to those at 0.2 ATM (Figure 16).

Of note in Fig. 15 are the species profiles and element fraction within about 1 mm from the surface. Considering the previous calculation of the stretching ratio, which is identified by the NO and HCN profiles, the distance of 1 mm corresponds to less than 100 μm for the result in Fig. 13. At the condition in Fig. 13, 100 μm was just above the resolution limit ($\sim$50 μm maximum) in the present TQMS system. The species profiles very near the surface in Figure 15 show some fluctuations, although the concentrations near the surface seemed to be similar to the results in Fig. 14. In Fig. 15, however, improved element balances in this region are obvious compared with the two previous results (Figs. 13 and 14), especially for H and O, due to the expansion of the primary reaction zone.

As a final result of the expansion of RDX chemical structure by lowering pressure, Fig. 16 shows species and element fraction profiles at 0.2 ATM and 400 W/cm^2. The length of the primary reaction zone was similar to that measured for 0.5 ATM; however, a more elongated reaction zone very near the surface was clearly found up to $\sim$0.8 mm from the surface. This region could be the reaction zone previously postulated by the Russian researchers; it is composed basically of the production/consumption of high-mass species (see Fig. 12), without any distinct changes of major species. Moreover, the result suggested that the region in Fig. 14, which was within $\sim$200 μm. It is noteworthy that the same kind of production of high-mass species was measured at the same condition in Fig. 12, with a more stretched production zone. The surface mole fraction of H_2CO increased from 7% to 11 and 12% as pressure decreased from 1 ATM to 0.5 and 0.2 ATM at 400 W/cm^2, showing that less of the H_2CO reacted to pro-

TABLE 2

Mole Fractions of Major Species Measured at the Surface

Test conditions	NO_2	HCN	N_2O	NO	N_2	H_2CO	CO	H_2O
1 ATM, 100 W/cm^2	0.04	0.23	0.09	0.21	0.06	0.03	0.08	0.22
1 ATM, 400 W/cm^2	0.16	0.23	0.08	0.14	0.04	0.03	0.07	0.22
.5 ATM, 400 W/cm^2	0.19	0.23	0.05	0.11	0.05	0.11	0.05	0.16
.2 ATM, 400 W/cm^2	0.20	0.23	0.06	0.08	0.06	0.12	0.06	0.18

duce H_2O and CO at the surface as pressure decreased.

Effects of the change of pressure and heat flux on RDX chemical structure should be reflected on all reaction regions in the flame; however, the most significant influence seems to be reflected near the deflagrating surface. Therefore, useful information could be obtained by comparing mole fractions of major species at the surface and analyzing the quantities relative to the change of pressure and heat flux. Mole fractions of major species measured on the surface are shown in Table 2 at various conditions. With the increase of heat flux from 100 to 400 W/cm^2 at a constant pressure of 1 ATM, no significant changes in the surface mole fractions were observed for the major species (except NO_2, which is favored at high heating rates, and NO, which is directly connected to NO_2). Two competing decomposition pathways of RDX have been suggested at the surface reaction zone as in (R3) and (R4) [37]. However, considering the high concentrations of H_2O, NO, CO, and N_2 at the surface in Table 2, it can be established that further decomposition of RDX beyond (R3) and (R4) already occurred at the surface. Therefore, at the present experimental conditions, reaction (R5) and (R6) should be included at the surface to explain all of the surface products and their quantities:

$$H_2CO + N_2O \rightarrow H_2O + CO + N_2 \qquad (R5)$$

$$2HONO \rightarrow H_2O + NO + NO_2 \qquad (R6)$$

Although (R5) is known to be prevalent at low heating rates and temperatures [74] and therefore is dominated by HCN and NO_2 under combustion-like conditions [37], it is clear that (R5) is occurring in this study due to the high mole fractions of CO and N_2 measured at the surface (see Table 2). The reaction (R6) had been previously suggested as the source of NO in the condensed phase [3, 75]. Another source of NO is NO_2 from a shift reaction between the two product species in (R6): $NO_2 \leftrightarrow NO + \frac{1}{2} O_2$ [14]. The inverse relationship of NO_2 and NO, which was measured in this study, due to their chemical coupling was also reported from an experimental study at high heating rates [14]. It is noteworthy that HCN does not participate in reaction (R5) and (R6) after its production from RDX at the present test conditions.

The effect of pressure change on major species at the surface is also shown in Table 2 at the fixed heat flux of 400 W/cm^2. From previous FTIR studies, it was reported that the initial concentrations of products and the decomposition mechanism of RDX essentially changed little with pressure over the range of 0.07–1 ATM [14, 18]. That finding may be partially supported by the present study since most of the major species in Table 2 show similar concentrations as pressure changes. However, from detailed comparison of the species data at various pressures, further information on RDX decomposition could be obtained at the surface. First, a significant increase of H_2CO is shown as pressure decreases; H_2CO may increase due to increased production from RDX decomposition or reduced conversion to CO via (R5). From the previous FTIR study of RDX thermolysis, it was reported that, as pressure decreases, a shift of gas products occurs from those resulting from C-N bond fission (condensed-phase decomposition) to products of N-N bond fission (gas-phase decomposition) [14]. However, this seems not to be applicable to the H_2CO trend in this study. Although it is not clear what the primary reasons might be for the different tendency of H_2CO, some explanations can be suggested.

Experiments in both the FTIR [14, 18] and present studies were conducted under an inert gas environment, at atmospheric pressure, with high heating rates; therefore, similar mole fractions are expected for the species evolved at the surface. However, in the FTIR studies at lower pressures, CO_2 existed as a major species with mole fraction comparable to that of NO, and the amount of N_2O was larger than that of HCN. Such results were not observed in the present measurements at any conditions (see Figures 13–16). Moreover, in this study, the major effect of the pressure decrease was also reflected in the expansion of the near-surface reaction zone. Since the surface position in this study was defined as the interface between the two-phase region on the surface and the gas phase, the mole fractions at the surface in Table 2 may better reflect species evolved in the two-phase region. The previous FTIR studies were performed under pyrolysis conditions for a small amount of RDX powder, while the present study was conducted under laser-assisted combustion for pellet-type RDX propellants. Therefore, the different experimental conditions may be contributing to the different H_2CO trends. There have been previous studies on various reaction pathways for producing H_2CO in the condensed phase at low pressures [3, 4, 7, 9, 18, 22]. However, those seem to be inadequate to directly explain the increase of H_2CO in this study, since most of the low-pressure studies were devoted to the RDX decomposition at selected pressures, not the changes with pressure decrease. Therefore, it is not clear why the pressure changes affect the mole fractions of H_2CO differently in the FTIR and the present study.

From RDX decomposition reactions (R3) and (R4), along with further reaction (R5) and (R6), NO, CO, and N_2 at the surface are expected to come from NO_2, H_2CO, and N_2O, respectively. Therefore, in terms of mole fractions, the decomposition of RDX at the surface can be reformulated as follows:

$$\tfrac{1}{3}\,\mathrm{RDX} \;\begin{cases} \nearrow\ H_2CO + N_2O \rightarrow [H_2CO + CO] + [N_2O + N_2] \\ \searrow\ HCN + HONO \rightarrow [HCN] + [NO_2 + NO] \end{cases} \qquad \text{(R7)}$$

where the parentheses were used to present the mole fraction of a species group with the same source. Table 2 can be reformulated regarding the species group in (R7):

Test conditions	$NO_2 + NO$	HCN	$N_2O + N_2$	$H_2CO + CO$	$H_2CO + \frac{1}{2} H_2O$
1 ATM, 400 W/cm^2	0.30	0.23	0.12	0.10	0.14
0.5 ATM, 400 W/cm^2	0.30	0.23	0.10	0.16	0.17
0.2 ATM, 400 W/cm^2	0.28	0.23	0.12	0.18	0.21

except for $[H_2CO + CO]$. The values of $[H_2CO + CO]$ at 1 and 0.5 ATM would appear to constant if the values of the alternative $[H_2CO + \frac{1}{2} H_2O]$ are considered. Therefore, where the last column of $[H_2CO + \frac{1}{2} H_2O]$ was added as an alternative expression for the same source of production as $[H_2CO + CO]$. The production of H_2O comes through (R5) and (R6), and the coefficient is an approximate value calculated by considering all pathways for the production. From this table, the mole fractions of each species group was found to be relatively constant at three different pressures RDX decomposition in the two-phase region seems to occur through the two competing branch reactions of (R3) and (R4), along with the subsequent reaction (R5) and (R6). It is noteworthy that the branching ratio between (R3) and (R4) in the two-phase region of RDX is about 2:1 at the present experimental conditions. Discrepancy of the mole fractions between the two components in each branch,

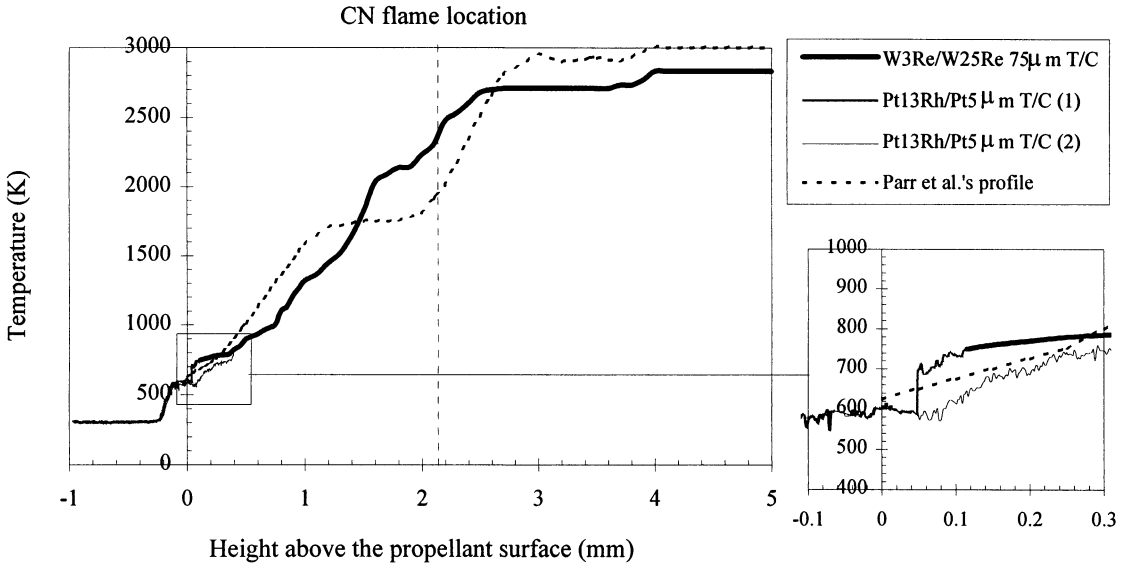

Fig. 17. Temperature profiles of deflagrating RDX at 1 atmosphere and 400 W/cm^2 in argon environment with various thermocouples. Parr and Hanson-Parr's temperature profile is from reference 33. Two profiles were scaled to the same CN flame distance in height.

[NO_2 + NO] and [HCN] for (R3), and [N_2O + N_2] vs. [H_2CO + CO] for (R4), may be explained either by other possible reactions that produced minor and high molecular weight products or by experimental errors.

Thermal Wave Structure

The investigation of the thermal wave structure of RDX flames constitutes an important part of broader investigations of the mechanism of RDX combustion. This study consists, quantitatively, of temperature profiles in combustion waves and at the burning surface and, qualitatively, of analysis of physical/chemical relationships of temperature and species profiles in the combustion wave. Therefore, temperatures in the gas and condensed phases of deflagrating RDX were measured to investigate the structure of thermal waves in RDX reaction zones and to study the relationship between thermal decomposition species and combustion waves.

Temperature profiles at 1 atmosphere and 400 W/cm^2 are shown in Fig. 17, along with Parr and Hanson-Parr's profile at a similar condition [24, 25, 33]. The profiles from the present study were composed of two different measurements with two different types of thermocouples: Pt/Rh- and W/Re-type thermocouples. In the measurements, regardless of diameters, Pt/Rh thermocouples could not survive whenever they passed through the CN flame where the temperature was ~2300 K. Therefore, W/Re thermocouples with diameters of 75 μm were used to obtain complete gas-phase temperature profiles up to the final flame. The two measurements were scaled to the same CN flame height.

In Fig. 17, the temperature at the surface was measured at 608 ± 15 K; however, the position was not clearly identifiable in this study, probably due to a relatively thick two-phase region at the surface (about 400 μm at this condition). The thermal wave thickness in the condensed phase was measured to be ~0.2 mm, while the thickness at 100 W/cm^2 was 1–1.5 mm. Although only two representative profiles are shown for the temperature near the surface and in the condensed phase, it should be mentioned that numerous measurements showed no distinct gradient change at the surface. A gradient change was observed in other studies at similar measurement conditions [24, 25, 33, 58], and the thick two-phase region in the present study seems to be the main reason for the lack of a clear gradient change. Connecting the two profiles required an adjustment due to a difference

in near-surface temperatures; under similar test conditions, the temperature difference between 5 and 75 μm thermocouples was measured to be ~100 K. After the adjustment, from the enlarged figure of the near-surface region in Fig. 17, it was found that the gradient change in the temperature profile occurred in the gas phase. However, based on other measurement attempts at the same condition, the connection may not be as steep as in the figure. The profile shows a relatively long region where the temperature increases very slowly from 750–850 K; this region had a height of up to 350–400 μm. Given the similar location of the high-mass species at the same condition (Fig. 12a), despite no direct evidence of its measurement in this study, this region is believed to be related to the decomposition reactions of RDX in the gas phase. The slowly increasing temperature region was followed by a steeper increase in temperature. Compared to the species profile at this condition (Fig. 14), the beginning of the region of temperature rise corresponds approximately to the end of major portion of NO_2 consumption and the start of NO and N_2O consumption. The CN flame was located at the end of the primary flame zone as shown in the figure (with a thin violet flame region in the video) and identified in the profile near the region where temperature increased more gradually beginning at ~2300 K. The temperature gradually increased to the final temperature (~2850 K) without any plateau zone. It is not clear if the final flame temperature measured here accurately represents the actual temperature, because the W/Re thermocouple began to glow just before passing through the CN flame due to heating and perhaps catalytic reactions. However, even considering these sources of error, the measured temperature seems reasonable since the calculated final temperature using an equilibrium code was ~3000 K.

Although the temperature profile from Parr and Hanson-Parr was measured using a combination of thermocouples and spectroscopic methods [24, 25, 33], the two profiles in Fig. 17 show extensive similarities: nearly the same surface temperatures, similar trends in the gas phase, and equivalent final reaction zone thickness. However, despite the similarities, the figure explicitly shows one major difference between the profiles, which results from the existence of the plateau zone or dark zone at the temperature of ~1750 K in Parr and Hanson-Parr's temperature profile. The species profiles measured in the same experiment [25] do not suggest the existence of the dark zone, since NO_2 and NO do not show regions of slow reaction at the same spatial location. However, for the profile in the present study where no plateau region was observed and temperature monotonically increases, the trend is consistent with the species measurement at the same condition (see Fig. 14). In the figure, where NO sustains its relatively constant concentration, some other major species are still involved in reactions through the consumption of HCN, N_2O, and H_2CO and the production of CO, N_2, CO_2, and H_2. Therefore, the reactions related to these species seem to produce enough energy to increase temperature with the constant NO mole fraction. The heat flux used in Parr and Hanson-Parr's experiment was ~600 W/cm^2 with the Gaussian beam shape of the CO_2 laser [25], thus yielding a maximum heat flux of ~1400 W/cm^2 at the center of propellant samples. From a modeling study, it was found that this high heat flux at the center of the sample was probably the major reason for the existence of the plateau zone in temperature profiles [76]. The difference of the final temperature between the two profiles is probably a result of different measurement methods: Parr and Hanson-Parr's profile was obtained using laser spectroscopic techniques [25]. Beyond the CN flame, some difficulties are normally experienced in temperature measurements with the thermocouple method, due primarily to the catalytic effects at high temperatures and radiative losses.

To investigate the effect of the pressure decrease on the thermal wave structure, other temperature measurements were conducted at 0.5 ATM and 400 W/cm^2. These were performed to study the thermal wave structure in the expanded near-surface reaction zones and confirm the method of interpreting the species profile based on the change of the CN flame distance, which was used by Parr and Hanson-Parr [25, 55]. The results are shown in Fig. 18, and some important and unexpected observations were made. Although the thermal wave structure was the same as that at 1 ATM and

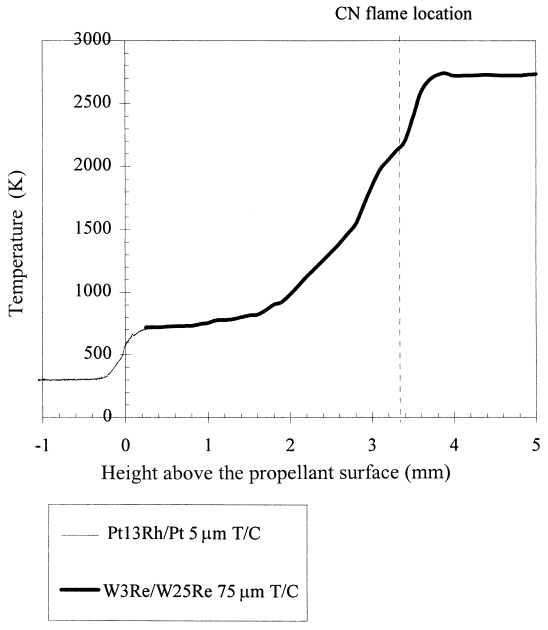

Fig. 18. Temperature profiles of deflagrating RDX at 0.5 atmosphere and 400 W/cm^2 in argon environment with two different thermocouples. Two profiles were scaled to the same CN flame distance in height.

400 W/cm^2, an unexpectedly long, slow growing temperature region was found near the surface up to ~1.8 mm. Although the CN flame standoff distance increased only from ~2.2 to ~3.2 mm with the change of pressure from 1 to 0.5 ATM at 400 W/cm^2, the slow growing region increased from ~0.4 to 1.8 mm. This long region of low temperatures was not measured in any previous studies and might be related to the expanded region of the production/decomposition of high mass species. However, the lower pressure did not lead to a plateau region before the CN flame. By comparison with the species profile at the same condition (Fig. 15), the slow growing zone represents the elongated portion of the primary flame zone.

In comparing Figs. 17 and 18, the temperature gradient in the secondary flame zone was increased from ~950 K/mm to ~1280 K/mm by lowering the pressure from 1 to 0.5 ATM. At the respective conditions, the distance for reaching a final temperature increased from ~3 to ~4 mm. Considering the distances of primary and CN standoff flames at both conditions, it is clear that, at lower pressures, the expansion ratio of a reaction zone was found to decrease as the distance from the propellant surface increased. This is probably due to a significant heat loss to the environment gas in the test chamber when the flame cross-sectional area expanded at a distance away from the burning surface at the low pressures. Therefore, the primary effect of lowering pressure at a constant heat flux was reflected in the expansion of primary flame zone thickness. These results suggest that the temperature profile scaling method of Parr and Hanson-Parr, which scales a temperature profile measured at one condition to a profile at another condition based only on the CN flame distance, should be applied with caution.

One important point should be made concerning the temperature profiles in the region from the surface to the starting point of the slow-growing temperature region. In Figures 17 and 18, the thickness of this region was ~100 μm at 1 ATM and increased to ~300 μm at 0.5 ATM, at the heat flux of 400 W/cm^2. Even though RDX vapor was not measured in this study, this region seems to be related to RDX decomposition since most of the high mass species tend to increase, or at least maintain their mole fractions, in this region for each condition (Fig. 12). The increase in high mass products was most obvious when pressure was lowered to 0.2 ATM (Fig. 12c), although no temperature data is available at this condition. From the present species data in which no direct measurements of RDX or its known fragments were made, it is not clear where the consumption of RDX ended in the gas phase. However, with the help of temperature measurements in Figs. 17 and 18, it might be postulated that RDX exists at least up to ~0.4 and ~1.6 mm from the surface at 1 ATM and 0.5 ATM and 400 W/cm^2, respectively. This analysis may be partially confirmed from the high mass species measurements at the same conditions in Fig. 12, where the consumption of most high mass species did not start until these distances, and related temperatures were slowly rising to these distances at these conditions.

Figure 19 shows surface temperature trends with the change of several parameters at the same experimental conditions of the species measurements in this study. In temperature

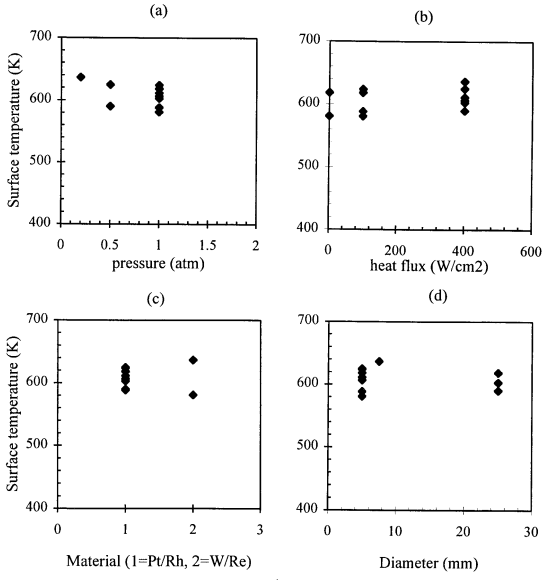

Fig. 19. The change of surface temperatures of deflagrating RDX at the condition of (a) heat flux of 400 W/cm^2, (b) pressure of 1 ATM, and (c) (d) 1 ATM and 400 W/cm^2 in argon environment.

measurements, the surface position has been identified by the point of curvature change of temperature profiles from the two-phase region to the gas phase, and by the first appearance of the thermocouple junction point on the deflagrating surface using a video camera. However, the first method was found to be inadequate for present measurements since the thickness of the two-phase region was too large for all pressure conditions to produce a distinct slope change at the surface. Therefore, all surface-temperature measurements in this study were obtained by the second method: comparing simultaneous traces of temperature and the photodiode signal recorded on a storage oscilloscope with the video images. The video system used recorded 30 images per second (therefore, sampling rate = 33 ms), and the sampling rate of temperature measurements using the oscilloscope could be obtained up to a single μsec. Due to the difference of sampling rates, there normally existed an uncertainty in accurately identifying the surface position during the temperature measurement through the oscilloscope recording. However, multiple measurements at a specific condition significantly increased reliability of the measured values. In Fig. 19a, surface temperatures at 400 W/cm^2 do not show any strong dependence on pressure change at these low pressure conditions, even though other high pressure experiments [56, 58] showed surface temperatures had a tendency to increase with pressures. The pressure insensitivity may be due to the high heat flux; 400 W/cm^2 is so high that RDX evaporation may be the dominant process in the two-phase region at the surface, thus the surface temperature is close to the (pseudo) boiling temperature of RDX [58, 77]. Therefore, the surface temperature seems to be relatively insensitive to pressure and other factors. The relatively thick two-phase region (350–500 μm at all experimental conditions) also reflects the active evaporation process of RDX at the surface. It may be noteworthy that surface temperatures in Figure 19b show a slight dependence on the change of heat flux at 1 ATM. In Fig. 19c, d, no change of surface temperatures was found as a result of a change in thermocouple materials and diameters. It is noteworthy to know that burning rates increased significantly with heat flux at a constant pressure, ~2.0 at 100 W/cm^2 to ~4.5 mm/sec at 400 W/cm^2 and 1 ATM, and increased with pressure at a constant heat flux, ~1 at 0.5 ATM to 2 mm/sec at 1 ATM and 400 W/cm^2 [51].

The constant surface temperature measured in this study was explained previously by the dominance of the RDX evaporation process at the surface. In the previous section of "Chemical Structure" in this study, it was noted that two global decomposition reactions of RDX, (R3) and (R4), occurred along with subsequent reactions such as (R5) and (R6) in the two-phase region. Therefore, if the chemical interaction exists at the surface, the species measured there should also be able to explain the temperature tendency. In an experimental study of species and temperature in the liquid phase, Brill and Brush found an intimate dependency of the N_2O/NO_2 ratio on temperature [78]. Regarding this result, Thynell et al. suggested reasonable modeling predictions of the N_2O/NO_2 ratio variation with temperature using available kinetic data [79]. In this study, the best modeling prediction of the N_2O/NO_2 ratio change with temperature (set 3 in Fig. 9, [78]) was used to understand the tendency toward constant surface temperatures using the species measured at

TABLE 3

Surface Temperatures (Ts) Calculated From the Species in Table 2 and the Prediction in [74]

Test conditions	$[H_2CO + CO]/[HCN]$	Ts	$[H_2CO + ½ H_2O]/[HCN]$	Ts	$[N_2 + N_2O]/[NO + NO_2]$	Ts
1 ATM, 100 W/cm^2	0.4571	639.22	0.6057	615.10	0.5664	620.77
1 ATM, 400 W/cm^2	0.4348	643.61	0.6087	614.70	0.4000	650.99
.5 ATM, 400 W/cm^2	0.6915	604.08	0.8271	589.47	0.3156	672.41
.2 ATM, 400 W/cm^2	0.8146	590.71	0.9430	579.01	0.4032	650.29

the surface in Table 2 within reasonable error bounds.

Surface temperatures that were calculated from the species in Table 2 are shown in Table 3; the calculations were performed with four species groups from the reformulated table for (R3) and (R4). Using the reformulated table seems to be more reasonable than using Table 2, because the species in Table 2 represent only one chemical snapshot in the two-phase region of the present study, compared with the temporal measurement from Brill and Brush [78], and the subsequent major reaction (R5) and (R6) are already occurring in the two-phase region. Thus, the reformulated table should be considered for more accurate predictions. In Table 3, where the calculation at 1 ATM and 100 W/cm^2 is also included for comparison, surface temperatures are reasonably constant at all conditions. The difference of the average surface temperature between measurement and calculation may be explained by the use of only global reactions in kinetic calculations. The "scatter" in the temperatures is acceptable, considering the uncertainty in the measured mole fractions. Therefore, the measurement of constant surface temperature in this study is consistent with the species at the surface.

SUMMARY AND CONCLUSIONS

The chemical and physical processes in the gas phase of RDX monopropellants were studied during laser-assisted combustion using a triple quadrupole mass spectrometer (TQMS), fine-wire thermocouple techniques, and a high-magnification video system. Using the full capability (parent and daughter modes) of the TQMS and careful calibration, it was possible to differentiate and quantify all species at the same mass to charge (m/z) value at 28 (N_2 and CO), 29 (CHO and H_2CNH), 30 (H_2CO and NO), and 44 (N_2O and CO_2). At $m/z = 29$, H_2CNH was found to exist as an actual decomposition product in the gas phase for the first time. Higher-molecular-weight species were found at m/z values of 47, 54, 56, 70, 81, and 97. By inspecting daughter ions from daughter mode experiments with the TQMS, the high mass species were estimated to be HONO, $C_2H_2N_2$, $C_2H_4N_2$, $C_2H_2N_2O$, $C_3H_3N_3$, and $C_3H_3N_3O$, and their chemical structures were suggested. By varying the ionization energy, it was found that the species at mass 47, 54, 70, 81, and 97 consist primarily of true decomposition products.

The measurement data on the species (which showed a reasonable closure in atom balances) and temperature profiles represent one of the most complete sets available for the chemical processes of RDX. These data show that increasing heat flux and decreasing pressure stretched out near-surface reaction zones; however, the conditions appeared to have no effect on the major reaction pathways in the gas phase. Also, the effects of pressure and heat flux changes were directly reflected in the surface chemistry. From the analysis of the surface mole fractions of major species, the RDX was found to experience both competing decomposition reactions into $H_2CO + N_2O$, (R3), and HCN + HONO, (R4), and subsequent reactions, $H_2CO + N_2O \rightarrow H_2O + CO + N_2$, (R5), and $2HONO \rightarrow H_2O + NO + NO_2$, (R6). With the consideration of all four reactions, a reasonable branching ratio of approximately 2:1 between (R3) and (R4) in the two-phase region of RDX was obtained at all experimental conditions. Due to the high temperature gradient very near the surface, Russian investigators [15, 45] had suggested that a very thin reaction zone might exist very near the surface of RDX, within 200

μm at 1 ATM. In the present work, the existence of this reaction zone, preceding the primary reaction zone, was observed in the species measurements at the lowest pressure of 0.2 ATM, and it seemed to be related to the production of NO_2 and production/consumption of high-mass species.

For all experimental conditions, the temperature profiles had a region where temperature increased very slowly near the surface. The thickness of this region was ~0.4 and ~1.8 mm at 1 and 0.5 ATM, respectively, under a heat flux of 400 W/cm^2 and increased as the near-surface reaction zone expanded. This region is believed to coincide with the production of NO and H_2O, consumption of NO_2 and H_2CO, and production/decomposition of high-mass species. After this region, the temperature increased to final flame temperatures without any temperature plateau corresponding to a dark zone. The surface temperature was measured to 608 ± 15 K and did not show any explicit dependence on the changes of thermocouple material or diameter, laser heat flux, or pressure. The interaction between chemical and thermal wave structures was explicitly identified by analyzing species and temperature profiles measured at the surface as well as in the gas phase. Constant surface temperature measured in this study was confirmed using a prediction based on the two global decomposition reactions of RDX in the liquid phase.

This work was performed under the sponsorship of the Office of Naval Research, Mechanics Division (ONR Contract No. N00014-93-1-0080). The support and encouragement of Dr. R. S. Miller are greatly appreciated. Dr. Tim Parr of NAWC generously contributed RDX powders for this study and provided many discussions that greatly improved the results of this work. The authors thank their colleague, Mr. Gautam Kudva, for his help with experiments.

REFERENCES

1. Bulusu, S., Weinstein, D. I., Autera, J. R., and Velicky, R. W., *J. Phys. Chem.* 90:4121–4126 (1986).
2. Stinecipher, M. M., *29th NANNAF Combustion Meeting*, CPIA Publ. No. 593, Vol. II, 1992.
3. Behrens, R. Jr, and Bulusu, S., *J. Phys. Chem.* 96:8877–8891 (1992).
4. Behrens, R. Jr, and Bulusu, S., *J. Phys. Chem.* 96:8891–8897 (1992).
5. Behrens, R. Jr, Land, T. A., and Bulusu, S., *30th JANNAF Combustion Meeting*, CPIA Publ. No. 606, Vol. II, 1993, pp. 47–59.
6. Rauch, F. C., and Fanelli, A. J., *J. Phys. Chem.*, 73(5):1604–1608 (1969).
7. Ermolin, N. E., Korobeinichev, O. P., Kuibida, and Fomin V. M., *Fizika Goreniya I Vzryva*, 22(5):54–64 (1986).
8. Cosgrove, J. D., and Owen, A. J., *Combust. Flame,* 22:13–22 (1974).
9. Farber M., and Srivastava, R. D., *Chem. Phys. Lett.*, 64(2):307–310 (1979).
10. Karpowicz, R. J., and Brill, T. B., *Combust. Flame*, 56:317–325 (1984).
11. Robertson, A. J. B., *Trans. Farady. Soc.* 45:85–93 (1949).
12. (a) Batten, J. J. and Murdie, D. C., *Aust. J. Chem.*, 23:737 (1970); (b) Batten, J. J. and Murdie, D. C., *Aust. J. Chem.*, 23:749 (1970); (c) Batten, J. J., *Aust. J. Chem.*, 24:945 (1971); (d) Batten, J. J., *Aust. J. Chem.*, 24:2025 (1971); (e) Batten, J. J., *Aust. J. Chem.*, 25:2337 (1972).
13. Zhao, X., Hintsa, E. J., and Lee, Y. T., *J. Chem Phys.*, 88(2):801–810 (1988).
14. Oyumi Y., and Brill, T. B., *Combust. Flame*, 62:213–224 (1985).
15. Korobeinichev, O. P., Kuibida, L. V., Orlov, V. N., Tereshchenko, A. G., Kutsenogii, K. P., Mavliev, R. V., Ermolin, N. E., Fomin V. M., and Emel'yanov I. D., *Mass-Spektrometry and Khim. Kinet.* (Tal'rose, V. L. Ed.), Moscow, Nauka, 1985, pp. 73–93.
16. Beard, B. C., *Propellants, Explosives, and Pyrotechnics*, 16:81–87 (1991).
17. Krause, H. H., Eisenreich, N, and Pfeil, A., *Propellants, Explosives, and Pyrotechnics*, 17:179–181 (1992).
18. Brill, T. B., Brush, P. J., Patil, D. G., and Chen, J. K., *24th Symposium (International) on Combustion*, The Combustion Institute, Pittsburgh, 1992, pp. 1907–1914.
19. Fetherolf, B. L., Liiva, P. M., Litzinger, T. A., and Kuo, K. K., *28th JANNAF Combustion Meeting*, CPIA Publ. 573, Vol. II, 1991, pp. 379–386.
20. Fetherolf, B. L., and Litzinger, T. A., *30th JANNAF Combustion Meeting*, CPIA Publ. 573, Vol. II, 1993, pp. 15–30.
21. (a) Wight, C. A., and Botcher, T. R., *J. Am. Chem. Soc.*, 114:8303–8304 (1992); (b) Botcher, T. R., and Wight, C. A., *Mat. Res. Soc. Symp. Proc.*, 296:47–51 (1993).
22. Melius, C. F., *Chemistry and Physics of Energetic Materials* (Bulusu, S. N., Eds.), Kluwer Academic Publishers, 1990, pp. 21–49.
23. Melius, C. F., *25th JANNAF Combustion Meeting*, CPIA Publ. 573, Vol. II, 1988, pp. 155–162.
24. Hanson-Parr D., and Parr, T., *26th JANNAF Combustion Meeting*, CPIA Publ. 529, Vol. I, 1989, pp. 27–37.
25. Hanson-Parr, D., and Parr, T., *25th Symposium (International) on Combustion*, The Combustion Institute, Pittsburgh, 1994, pp. 1635–1643.

26. Oyumi, Y., and Brill, T. B., *Combust. Flame*, 66:9–16 (1986).
27. Brill, T., *Mat. Res. Soc. Symp Proc.*, 296:269–280 (1993).
28. Fifer, R. A., in *Fundamentals of Solid–Propellant Combustion* (Kuo, K. K. and Summerfield, M., Eds.) Progress in Astronautics and Aeronautics Vol. 90, AIAA Inc., New York, 1984, pp. 177.
29. Boggs, T. L., in *Fundamentals of Solid–Propellant Combustion* (Kuo, K. K. and Summerfield, M., Eds.) Progress in Astronautics and Aeronautics Vol. 90, AIAA Inc., New York, 1984, pp. 121.
30. Brill, T. B., *Prog. Energy Combust Sci.*, 18:91–116 (1992).
31. Parr, T. and Hanson-Parr, D., *31st JANNAF Combustion Meeting*, CPIA Publ. 620, Vol. II, 1994, pp. 407–423.
32. Parr, T. and Hanson-Parr, D., *28th JANNAF Combustion Meeting*, CPIA Publ. 573, Vol. III, 1991, pp. 359–368.
33. Parr, T. and Hanson-Parr, D., *32nd JANNAF Combustion Subcommittee Meeting*, CPIA Publ. 631, Vol. I, 1995, pp. 429–437.
34. Lee, Y. J., Tang, C.-J., and Litzinger, T. A., *31st JANNAF Combustion Meeting*, CPIA Publ. 620, Vol. II, 1994, pp. 425–437.
35. Lee, Y. J., Tang, C. J., and Litzinger, T. A., *32nd JANNAF Combustion Subcommittee Meeting*, Huntsville, AL, 1995.
36. Ermolin, N. E., Korobeinichev, O. P., Kuibida, and Fomin V. M., *Fizika Goreniya I Vzryva*, 24(4):400–407 (1988).
37. Brill, T. B., *J. Propul. and P*, 11(4):740–751 (1995).
38. Li. S. C., Williams, F. A., and Margolis, S. B., *Combust. Flame*, 80(3,4):329–349 (1990).
39. BenReuven, M, Caveny, L. H., Vichnevetsky, R. J., and Summerfield, M., *16th Symposium (International) on Combustion*, The Combustion Institute, Pittsburgh, 1976, pp. 1223–1233.
40. Melius, C. F., and Binkley, J. S., *21st Symposium (International) on Combustion*, The Combustion Institute, Pittsburgh, 1986, pp. 1953–1963.
41. Li. S. C., and Williams, F. A., *J. Propul P*, 12(2):302–309 (1996).
42. Litzinger, T. A., Fetherolf, B. L., Lee, Y. J., and Tang, C.-J., *J Propul P*, 11(4):698–703 (1995).
43. Korobeinichev, O. P., and Kuibida, L. V., in *Flames, Lasers, and Reactive Systems*, 8th Int. Colloquium on Gas Dynamics of Explosives and Reactive Systems, Minsk, USSR, 1981.
44. Parr, T., and Hanson-Parr, D., *Spring Meeting of the Western States Section/The Combustion Institute*, The Combustion Institute, Paper 87–88, 1987.
45. Ermolin, N. E., Korobeinichev, O. P., Tereshenko, A. G., and Fomin V. M., *Combustion, Explosion, and Shock Waves*, 18(1):36–38 (1982).
46. Korobeinichev, O. P., *Combustion, Explosion, and Shock Waves*, 23(5):565–576 (1987).
47. Howard, S. L., Locke, R. J., Sausa, R. C., Dayton, D. C., Barts, S. A., and Miziolek, A. W., *28th JANNAF Combustion Meeting*, CPIA Publ. 573, Vol. II, 1991, pp. 527–532.
48. Busch, K. L., Glish, G. L., and McLuckey, S. A., *Mass Spectrometry/Mass Spectrometry*, VCH Publishers Inc., New York, 1988.
49. (a) Heitor, M. V. and Moreira, A. L. N., *Prog. Energy Combust Sci.*, 19:259–278 (1993); (b) Cernansky, N. P. and Sawyer, R. F., *15th Symposium (International) on Combustion*, The Combustion Institute, Pittsburgh, PA, 1975, pp. 1039–1050; (c) Cernansky, N. P., *AIAA 15th Aerospace Science Meeting*, Washington, D.C., January 26–28, AIAA Paper No. 76–139, 1976; (d) Kramlich, J. C. and Malte, P. C., *Comb. Sci. Tech.*, 18:91–104 (1978); (e) Schoenung, S. M. and Hanson, R. K., *Comb. Sci. Tech.*, 24:227–237 (1981).
50. *Eight Peak Index of Mass Spectra*, Vol. 2, Third Edition, The Royal Society of Chemistry, 1983.
51. Lee, Y. J., The Pennsylvania State University, Department of Mechanical Engineering, Ph.D. Thesis, 1996.
52. Bobeldijk, M., Van der Zande, W. J., and Kistemaker, P. G., *Chemical Physics*, 179:125–130 (1994).
53. (a) Kieffer, L. J., and Dunn, G. H., *Review of Modern Physics*, Vol. 38, No. 1, American Physical Society, 1996, pp. 1–35; (b) Tawara, H., and Kato, T., *At. Data Nucl. Data Tables*, 36:167 (1983).
54. *CRC Handbook of Chemistry and Physics*, 66th ed., CRC Press, 1985–86.
55. Hanson-Parr, D., and Parr, T., *28th JANNAF Combustion Meeting*, CPIA Publ. 573, Vol. II, 1991, pp. 369–378.
56. Zenin, A., A Presentation in the URI Seminar Series, The Penn. State Univ., 1994.
57. Zenin A. A., in *Nonsteady Burning and Combustion Stability of Solid Propellants* (DeLuca L., Price, E. W., and Summerfield, M., Eds.), Progress in Astronautics and Aeronautics Vol. 143, AIAA, Washing DC, 1992, pp. 197–231.
58. Zenin A., *J Propul P*, 11(4):752–758 (1995).
59. Fristrom, R. M., and Westenberg, A. A., *Flame Structure*, McGraw-Hill Books, New York, 1965.
60. *Thermocouple Reference Tables*, Omega Engineering, Inc., 1993.
61. (a) Chedaille, J. and Braud, Y., *Industrial Flames, Vol. 1, Measurements in Flames* (Beer, J. M. and Thring, M. W., Eds.) International Flame Research Foundation, Edward Arnold Ltd., London, 1972; (b) Incropera, F. P. and DeWitt, D. P., *Fundamentals of Heat and Mass Transfer*, 3rd edition, John Wiley & Sons, 1990.
62. Zenin A. A., *Pure and Appl. Chem.*, 62(5):889–897 (1990).
63. Fetherolf, B. L., *The Physical and Chemical Processes Governing CO_2 Laser-Induced Pyrolysis and Combustion of the Solid Propellants RDX, ADN, XM39, and M43*, The Pennsylvania State University, Department of Mechanical Engineering, Ph.D. Thesis, 1994.
64. Tsang, W., *30th JANNAF Combustion Meeting*, CPIA Publ. 606, Vol. II, 1993, pp. 297–305.
65. Farber M., and Srivastava, R. D., *Chem. Phys. Letters*, 80(2):345–349 (1981).
66. Behrens, R. Jr, *Int J Chem Kinet*, 22:135–157 (1990).
67. Korobeinichev, O. P., Kuibida, L. V., and Pletskii,

A. A., *Conference on Applications of Free-Jet, Molecular Beam Mass Spectrometric Sampling*, National Renewable Energy Institute and Extrel, Estes Park, CO, 1994.
68. Schroeder, M. A., *Critical Analysis of Nitramine Decomposition Data: Product Distributions from HMX and RDX Decomposition*, Technical Report BRL-TR-2659, 1985.
69. Tang, C.-J., *A Study of the Steady Chemical Structure of HMX Flame and Combustion Response to Oscillatory Heat Flux*, The Pennsylvania State University, Department of Mechanical Engineering, The Pennsylvania State University, Department of Mechanical Engineering, Ph.D. Thesis, 1997.
70. Liau, Y.-C. and Yang, V., *J. Propul. P.*, 11(5):729–739 (1995).
71. Schroeder, M. A., *17th JANNAF Combustion Meeting*, CPIA Publ. No. 329, Vol. II, 1980, pp. 493–508.
72. Tang, C. J., Lee, Y. J., and Litzinger, T. A., *31st JANNAF Combustion Meeting*, CPIA Publ. 620, Vol. II, 1994, pp. 307–316.
73. Lee, Y. J., Tang, C. J., and Litzinger, T. A., *ARO/URI Program Review*, 1994.
74. (a) Fifer, R. A. and Holmes, H. E., *16th JANNAF Combustion Meeting*, CPIA Publ. 308, Vol. II, 1979, pp. 35–50; (b) Ben-Reuven, M. and Caveny, L. H., *AIAA Journal*, 19:1276–1285 (1979).
75. Fifer, R. A., *J. Phys. Chem.*, 80:2717 (1976).
76. Prasad, K, Yetter, R. A., and Smooke, M. D., *Comb. Sci. Tech.*, 124:35 (1997).
77. Davidson, J. E. and Beckstead, M. W., *J. Propul. P.*, 13(3):375–383 (1997).
78. Brill, T. B., and Brush, P. J., *Phil. Trans. R. Soc. Lond. A*, 339:377–385 (1992).
79. Thynell, S. T., Gongwer, P. E., and Brill, T. B., *J. Propul. P.*, 12(5):933–939 (1996).

Received 9 February 1998; accepted 18 August 1998